

LA-UR-24-28494

Accepted Manuscript

Preferential adsorption of noble gases in zeolitic tuff with variable saturation: A modeling study of counter-intuitive diffusive-adsorptive behavior

Ortiz, John Philip
Neil, Chelsea Wren
Rajaram, Harihar
Boukhalfa, Hakim
Stauffer, Philip H.

Provided by the author(s) and the Los Alamos National Laboratory (1930-01-01).

To be published in: Journal of Environmental Radioactivity

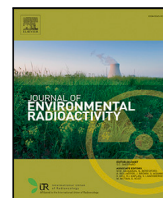
DOI to publisher's version: 10.1016/j.jenvrad.2024.107608

Permalink to record:

<https://permalink.lanl.gov/object/view?what=info:lanl-repo/lareport/LA-UR-24-28494>



Los Alamos National Laboratory, an affirmative action/equal opportunity employer, is operated by Triad National Security, LLC for the National Nuclear Security Administration of U.S. Department of Energy under contract 89233218CNA000001. By approving this article, the publisher recognizes that the U.S. Government retains nonexclusive, royalty-free license to publish or reproduce the published form of this contribution, or to allow others to do so, for U.S. Government purposes. Los Alamos National Laboratory requests that the publisher identify this article as work performed under the auspices of the U.S. Department of Energy. Los Alamos National Laboratory strongly supports academic freedom and a researcher's right to publish; as an institution, however, the Laboratory does not endorse the viewpoint of a publication or guarantee its technical correctness.



Preferential adsorption of noble gases in zeolitic tuff with variable saturation: A modeling study of counter-intuitive diffusive-adsorptive behavior

John P. Ortiz ^{a,b}, Chelsea W. Neil ^a, Harihar Rajaram ^b, Hakim Boukhalfa ^a, Philip H. Stauffer ^a

^a Earth and Environmental Sciences Division, Los Alamos National Laboratory, Los Alamos, 87545, NM, USA

^b Department of Environmental Health and Engineering, The Johns Hopkins University, Baltimore, 21218, MD, USA

ARTICLE INFO

Keywords:

Underground nuclear explosions
Diffusion
Adsorption
Zeolites
Variable saturation
Nonproliferation
Noble gases

ABSTRACT

Noble gas transport through geologic media has important applications in the prediction and characterization of measured gas signatures related to underground nuclear explosions (UNEs). Retarding processes such as adsorption can cause significant species fractionation of radionuclide gases, which has implications for measured and predicted signatures used to distinguish radioxenon originating from civilian nuclear facilities or from UNEs. Accounting for the effects of variable water saturation in geologic media on tracer transport is one of the most challenging aspects of modeling gas transport because there is no unifying relationship for the associated tortuosity changes between different rock types, and reactive transport processes such as adsorption that are affected by the presence of water likewise behave differently between gas species. In this study, we perform numerical diffusive-adsorptive transport simulations to estimate gas transport parameters associated with bench-scale laboratory diffusion cell experiments measuring breakthrough in zeolitic and non-zeolitic rocks for a gaseous mixture of xenon, krypton, and SF₆ at varying degrees of water saturation (S_w). Counter-intuitive transport behavior was observed in the zeolitic rock experiments whereby breakthrough concentrations were significantly higher when the core was partially saturated ($S_w = 17\%$) than under dry ($S_w = 0\%$) conditions. Breakthrough of xenon was especially retarded in the dry core – likely due to comparatively high affinity of xenon for zeolitic adsorption sites – and estimated effective diffusion coefficients for all gases were approximately an order of magnitude lower than what is predicted by porosity-tortuosity models. We propose the counter-intuitive behavior observed is because water infiltration of zeolite nanopores reduces both the adsorptive capacity of the rock and the tortuosity of connected flow paths. We developed a two-site competitive kinetic Langmuir adsorption reaction for the porous media transport simulator in order to constrain transport parameters within zeolitic tuff, where differential adsorption to zeolite and non-zeolite pores was observed. We determined that liquid saturation-dependent diffusive-adsorptive transport is affected by subtle and at times competing processes that are specific to different gases, which have a significant overall influence on effective transport parameters.

1. Introduction

Gas transport through variably-saturated geologic media has important applications for nuclear nonproliferation, as noble gas detection is one of the best candidates for the verification of clandestine underground nuclear events (Auer et al., 1996; Bourret et al., 2019; Carrigan et al., 1996; Sun and Carrigan, 2014; Kalinowski, 2011). Underground nuclear explosions produce gaseous radionuclides (such as xenon) via nuclear fission, which tend to migrate upwards from the cavity to the surface. Vertical transport of subsurface gases can be enhanced by barometric pumping, a mechanism whereby atmospheric pressure fluctuations push and pull gases within fractured rock (Nilson

et al., 1991). Over multiple cycles of pressure variations, the fracture-matrix exchange between rapid fracture flow and temporary storage via diffusion into the rock matrix produces a ratcheting mechanism that can greatly enhance upward gas transport relative to advection and diffusion alone (Harp et al., 2018; Massmann and Farrier, 1992; Neepner and Stauffer, 2012a,b; Nilson et al., 1991; Takle et al., 2004; Ortiz et al., 2022; Avendaño et al., 2021; Stauffer et al., 2019). If these gases release into the atmosphere, they can potentially be detected via atmospheric monitoring, which makes them a key component to compliance monitoring and treaty verification for the comprehensive nuclear-test-ban treaty (CTBT) (Carrigan and Sun, 2014; Jordan

* Corresponding author at: Earth and Environmental Sciences Division, Los Alamos National Laboratory, Los Alamos, 87545, NM, USA.

E-mail address: jportiz@lanl.gov (J.P. Ortiz).

URL: <https://johnportiz14.github.io/> (J.P. Ortiz).

<https://doi.org/10.1016/j.jenrad.2024.107608>

Received 26 August 2024; Received in revised form 6 December 2024; Accepted 22 December 2024

Available online 1 January 2025

0265-931X/© 2024 The Authors. Published by Elsevier Ltd. This is an open access article under the CC BY license (<http://creativecommons.org/licenses/by/4.0/>).

et al., 2014). Accurate prediction of subsurface noble gas transport is challenging because of significant uncertainty and heterogeneity in subsurface geological materials. In addition, we lack detailed understanding of certain key processes that control transport, including the effects of variable degrees of water saturation in the rock on the effective diffusion coefficients of gas tracers, and the adsorption of noble gases onto geological materials such as zeolites. The interaction of such processes can sometimes lead to highly counter-intuitive behavior that can confound efforts to characterize transport.

Gas transport within a porous medium behaves differently than when the gas is in the presence of air alone. Within a porous medium, such as rock or soil, the cross-sectional area available for diffusive transport is reduced due to the presence of solids (i.e., the rock walls). Transport takes place within interconnected pores inside the rock, which adds varying degrees of tortuosity to the travel path of the gas molecules. The presence of water in the pores additionally complicates transport, as this further reduces the available volume of air in which vapor-phase diffusion can occur. In partially saturated porous media, the effective diffusion coefficient of a gas can be expressed as a function of volumetric water content because the random motions of the gas tracer that cause diffusion are restricted to increasingly tortuous pathways as water content increases (Stauffer et al., 2009):

$$D_e = D_0 \frac{(\phi \cdot (1 - S_w))}{\tau} = D_0 \frac{\theta_a}{\tau} = D^* \theta_a \quad (1)$$

where D_e is the effective vapor diffusion coefficient [$\text{m}^2 \text{s}^{-1}$]; D_0 is the free-air diffusion coefficient [$\text{m}^2 \text{s}^{-1}$]; D^* is the porous-medium diffusion coefficient [$\text{m}^2 \text{s}^{-1}$], a quantity defined as $D^* = \frac{D_0}{\tau}$ that accounts for the tortuosity of the porous medium; τ is the tortuosity [-; m/m], the dimensionless ratio between the average length of a particle streamline through porous media to the straight-line distance between those points; θ_a is the volumetric air content [-; m^3/m^3], defined as the volume of air divided by the total volume of rock (alternatively, $\theta_a = (1 - S_w)\phi$, where S_w is water saturation [-; m^3/m^3]; and ϕ is the porosity [-; m^3/m^3]. Several theories have been derived to relate the effective diffusion coefficient and water saturation (Conca and Wright, 2000; Millington and Quirk, 1961). Perhaps the one most commonly used is the Millington-Quirk (hereafter MQ) model, a tortuosity-based relationship originally reported in Millington and Quirk (1961) and modified by Jury et al. (1991). Though originally written to relate effective liquid-phase diffusion coefficients in variably saturated rock, it is extended to vapor-phase diffusion as:

$$D_e^{MQ} = \frac{D_0 \theta_a^{10/3}}{\phi^2} \quad (2)$$

where D_e^{MQ} is the MQ effective diffusivity [$\text{m}^2 \text{s}^{-1}$], and the other variables have been defined previously in Eq. (1). The MQ model has been shown to be in good agreement with data over a range of soil/rock water content in a number of different studies (Stauffer et al., 2009; Sallam et al., 1984; Jordan et al., 2014; Baehr, 1987) when considering solute diffusion in liquid. However, the MQ model is derived from theory using several assumptions, and therefore cannot be expected to apply to every rock type and scenario. In fact, the existence of a generalized, unique relationship between relative diffusivity in soil/rock and volumetric water content has been rejected by some researchers (Bruckler et al., 1989). MQ assumes an “ideal” porous medium; that is, there is a general absence of anisotropy or cementation, and that there is a complete distribution of pore sizes. Jin and Jury (1996) found that for gases in soils, other models may provide a better fit to experimental data. Despite its shortcomings, the MQ model is widely used by the porous media flow and transport community as the *de facto* model for transport parameters in variably saturated media.

Adsorption is a phenomenon in which gas or liquid tracer molecules (the “adsorbate”) adhere to the surface of another material (the “adsorbent”). Gas molecule transport through porous media is retarded by adsorption onto the pore walls. Adsorption is aided by adsorbents with high specific surface area, which have more sites onto which gas

molecules can adsorb. Furthermore, adsorption reactions are generally exothermic processes, meaning that lower temperatures facilitate the adsorption of gas particles onto the adsorbent, while higher temperatures favor desorption (Adamson, 1979; Pick, 1981). Adsorption of gas molecules can occur to varying degrees on many different rock types or surfaces, and laboratory studies have shown non-trivial xenon adsorption on rock types such as shale, dolomite, limestone, and sand Paul et al. (2018a,b), Byers et al. (2019). The kinetics and total amount of adsorption depend ultimately on the affinity of the adsorbate for the adsorbent, the concentration of the adsorbate above adsorbent material, and the availability of adsorption sites on the adsorbent (Breck, 1974).

One geologic material that is highly effective as an adsorbent is zeolites. Zeolites are crystalline aluminosilicate materials that form microporous frameworks resembling cages. Synthetic zeolites are commonly used as commercial adsorbents due to their effectiveness at trapping and thereby separating molecules by size, but they also occur naturally in some volcanic rocks and ash layers. Volcanic zeolites have even been hypothesized as a potential reservoir for subsurface methane on Mars because the zeolitic trapping could act as a fast sink that may explain short-term atmospheric methane variations observed at Gale crater (Holmes et al., 2015; Mousis et al., 2016; Ortiz et al., 2024; Ortiz, 2024). A recent study found that natural zeolites in zeolitic tuff can adsorb noble gases, and in particular, xenon (Feldman et al., 2020). Understanding the degree to which certain gases are adsorbed during subsurface transport is critical to understanding measured tracer signatures, as retardation of some gases relative to others will lead to signature fractionation (Johnson et al., 2019; Ackley et al., 2003; Dutta and Bhatia, 2018). Many historical US underground nuclear tests were conducted in zeolite-rich subsurface units (e.g., zeolitic tuff) within Pahute Mesa at Nevada National Security Site (NNSS) (Moncure et al., 1981). It is therefore important to understand the effects of zeolites on gas subsurface transport to better interpret and model historical gas transport data.

Previous research has measured adsorption parameters and diffusivity of Xe and SF₆ through zeolitic tuff via laboratory investigations using dry and partially-saturated rock cores (Paul et al., 2020; Feldman et al., 2020). However, measurements of diffusivity for the partially-saturated zeolitic tuff took place under nearly fully saturated conditions (Paul et al., 2020). A recent study used molecular dynamics simulations to quantify noble gas mobility and adsorptive mass loading within zeolites under dry and partially saturated conditions (Greathouse et al., 2023), though the analysis focused on nano-scale processes in pure zeolites, which do not always scale cleanly to micro- and meso-scale transport in non-pure zeolitized rock samples. We therefore do not have any comprehensive previous studies measuring the effects of multiple degrees of partial saturation on gas transport through zeolitic tuff covering the range between 0% and 100% water saturation. Recent work by our team (Neil et al., 2022a) measured noble gas (Xe, Kr, SF₆) diffusion through variably saturated zeolitic and non-zeolitic tuff cores using bench-scale diffusion cell experiments. In zeolitic tuff, we observed unexpected gas breakthrough behavior; gas transport was greatly retarded in the dry ($S_w = 0\%$) core relative to the partially saturated cases, most noticeably for Xe (Neil et al., 2022a). From MQ theory, we would expect the opposite behavior. In non-zeolitic tuff, we observed the expected behavior (progressively slower gas breakthrough as water is added) for gas diffusion, which lead us to hypothesize that the presence of water reduced the uptake of gases by the zeolites by blocking adsorption sites as the pores were filled. This hypothesis was partially corroborated by small-angle neutron scattering (SANS) measurements performed on the zeolitic tuff samples (Fig. 5 in Neil et al., 2022a). The SANS measurements showed preferential filling of pore sizes suspected to be zeolite as small amounts of water were added to the sample (Figures S1, S2), which implies that adding water to the rock will block access to the zeolites and reduce gas adsorption,

thereby resulting in reduced adsorptive retardation at higher liquid saturation.

The goal of the current study is to interrogate the experimental results and analysis reported in Neil et al. (2022a) using numerical models of reactive gas transport in porous media. We couple reactive transport simulations with an exhaustive parameter estimation approach to interpret relevant gas transport parameters through variably-saturated zeolitic rock. We implement a dual-site kinetic adsorption process in our diffusive transport simulations to account for retardation within our conceptual model of zeolitic pore adsorption. We found such a model to be the only way to reproduce the transport observed in our diffusion cell experiments for variably-saturated zeolitic rocks.

The transport properties of porous geologic media with respect to such gases are of fundamental importance in developing accurate predictive transport models to determine the origin of detected nuclear signatures in variably-saturated media. Our results demonstrate the medium-specific nature of tracer transport in porous media, and the relatively unique and counter-intuitive manner with which pore water can affect transport in atypical substrates.

2. Materials & methods

This study uses numerical adsorption-diffusion modeling to estimate gas transport parameters of xenon, krypton, and sulfur hexafluoride (SF_6) within variably saturated zeolitic tuff cores ($S_w = 0\%$, 17% , 40% , and 85%). The models are informed by gas breakthrough results obtained via bench-scale laboratory diffusion cell experiments that were originally presented in our previous work (Neil et al., 2022a). Neil et al. (2022a) also performed similar diffusion cell experiments with the same setup for a non-zeolitic tuff (at $S_w = 0\%$ and 27%) and sandstone ($S_w = 0\%$) for comparison. The experimental setup is described briefly below, though the reader is referred to Neil et al. (2022a) for detailed experimental methods.

2.1. Experiments

2.1.1. Rock core samples

Zeolitic tuff core samples were obtained from the UE-20az-NG-4 core hole on Pahute Mesa at the NNSS at a depth of 440.65 – 440.83 m. The lithologic unit at this depth is zeolitic non-welded tuff from the Calico Hills zeolitic composite unit (Bouret et al., 2020). Porosity along this unit was measured using helium porosimetry and was found to vary between 16.7% and 32.7%, with an average porosity of 21.6%. The cores were cut to 5.1 cm in length and had a diameter of 6.2 cm. More details about the core samples can be found in Neil et al. (2022b).

The non-zeolitic tuff core samples were from the Bandelier Tuff unit (Qbt2) from Los Alamos, NM. Mean porosity was 36.0%. The core was 5.1 cm in length and had a diameter of 5.08 cm.

The sandstone core sample was obtained from the Castlegate sandstone formation. Mean porosity was 28.0%. The core was 11.9 cm in length and had a diameter of 4.46 cm.

2.1.2. Diffusion cell setup

After the cylindrical rock core was cut into sections, the circular faces were trimmed to ensure flat, uniform faces in contact with either side of the diffusion cell. The non-face radial edges of the core were coated with a UV-curable polymer (UV15X-6NONMED-2, Master Bond, Inc., Hackensack, NJ, USA) to prevent gas escape or migration along the radial edge of the samples, thereby ensuring primarily longitudinal transport along the axis of the cylindrical core. This method for sealing the rock core has been described previously by our group (Neil et al., 2022a) and was shown to be impermeable to Kr, Xe, and SF_6 .

The core was buttressed on both ends by empty cylindrical reservoirs machined out of plexiglass. The large reservoir (which contained the initial “spiked” gas mixture) has a volume of 500 mL, while the smaller reservoir has a volume of 75 mL. When the experiment begins,

the gas mixture diffuses from the large reservoir into the core and subsequently enters the smaller reservoir. Both reservoirs have two sampling ports that lead to the mass spectrometer.

Gas concentrations are measured using a Pfeiffer Vacuum OmniStar GSD 320 mass spectrometer (Pfeiffer Vacuum, Aßlar, Germany). The mass spectrometer (MS) is attached to one of the sampling ports of both reservoirs through a Valco dead-end selector valve and a needle is placed in the other port to prevent the formation of a vacuum while the MS samples at a rate of approximately 0.40 mL/min. To minimize the volume of gas sampled, the selector valve was programmed to allow intermittent sampling of the diffusion cell. Sampling over the 20 h period dilutes the gas concentration, which is accounted for in the numerical model via specified flow-rate boundary conditions at inflow and outflow nodes. In addition, regular monitoring of concentration in both the spiked and sampled chambers provides a view of the changing driving forces for diffusion with time as the system is sampled.

To begin the experiment, the large reservoir was spiked, which contains ambient air, with 1 mL each of stable xenon (Xe), krypton (Kr), and SF_6 tracers while measuring their ion current, which correlates with their masses on the spectrometer. This injected volume corresponds with a concentration of 2000 parts per million by volume (ppmv) for each of the three gases.

The sampling process is automated such that the small reservoir is measured for 1 min every 10 min to monitor breakthrough and the spiked reservoir is measured for 2 min every hour to monitor changes in the inlet concentration. A magnetic stirrer continually mixes the spiked cell to maintain a homogeneous gas mixture and prevent gravity separation of the gases. The zeolitic tuff diffusion cell experiments were run separately for five different degrees of saturation: 0% (dry, unsaturated), 17%, 40%, and 85%. The non-zeolitic tuff diffusion cell experiments were performed at 0% and 27% saturation, while the sandstone diffusion cell experiment was performed at 0% saturation (dry). The reader is referred to Neil et al. (2022a) for a detailed description of the saturation process, which was performed to ensure uniform water distribution within the core sample.

2.2. Diffusion-adsorption modeling

We simulate gas tracer transport through the rock core with a diffusion-adsorption model using a 1-D axially-symmetric geometry. We then use a parameter optimization routine to determine the range of transport parameters that minimize the error of the calculated breakthrough concentrations compared to the experimentally derived values.

2.2.1. Kinetic dual-site Langmuir adsorption

The Langmuir adsorption model has been used to describe adsorption for a variety of tracers. In the simplest case – one adsorbing species (adsorbate) onto a series of equivalent sites on the surface of the solid (adsorbent) – the model is valid given the following assumptions: (1) the surface with the adsorbing sites is perfectly flat and homogeneous, (2) the adsorbing gas adsorbs into an immobile state, (3) all sites are energetically equivalent, (4) each site can hold at most one molecule of the adsorbing species (i.e., monolayer coverage only), and (5) no interactions occur between adsorbate molecules at adjacent sites. In the slightly more complex case of competitive adsorption between multiple adsorbing species, assumption #4 is modified in that each site can hold at most one adsorbing molecule, and cannot hold multiple species simultaneously.

The general competitive Langmuir adsorption rate law for the change in concentration of vapor species j is given by:

$$\frac{\partial C_j}{\partial t} = -\frac{\rho}{\phi} k_m \left(K_L C_j \left(s_j^{max} - \sum_{n=1}^{\infty} \left(s_n \cdot \frac{\sigma_n}{\sigma_j} \right) \right) - s_j \right) \quad (3)$$

where C_j is the vapor-phase concentration of constituent j [mol kg_r^{-1}], t is time [s], k_m is the mass transfer rate constant [s^{-1}], K_L is the Langmuir distribution coefficient [$\text{kg}_v \text{mol}^{-1}$], s_j^{max} is the maximum

adsorbed concentration of j on the rock [mol kg_r^{-1}], s_j is the adsorbed concentration (solid phase) of constituent j [mol kg_r^{-1}], σ_j is the molecular area [m^2] of the adsorbed species j , and the summation term takes place over all participating/competing gas species n . Assuming that the maximum adsorbable concentration is a monolayer (surface coverage $\Theta = \frac{s_j}{s_j^{\max}} = 1 = \Theta_{\text{mono}}$), it can be calculated as: $s_j^{\max} = \frac{\text{SSA}}{N_A \sigma_j}$, where SSA is specific surface area [$\text{m}^2 \text{kg}_r^{-1}$] and N_A is Avogadro's constant. From Eq. (3), it is evident that the sites available for adsorption (s_j^{\max}) of a given species j can be occupied by any/all of n total species (in the present work: Xe, Kr, SF₆). The adsorption model presented in Eq. (3) is used to simulate the diffusion cell experiments for the non-zeolitic tuff and sandstone samples.

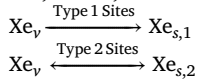
To represent separate adsorption processes occurring on the walls of zeolitic pores in addition to normal rock pores (i.e., for the zeolitic tuff), we require a more complex model. In the case of dual-site competitive adsorption, the vapor-phase constituent partitions separately into the adsorbed (solid) phase at both Type 1 and Type 2 sites. In our model, we conceptualize the rate of vapor species j concentration change as:

$$\frac{\partial C_j}{\partial t} = -\frac{\rho}{\phi} \left[(\text{net Type 1 desorption rate}) + (\text{net Type 2 desorption rate}) \right] \quad (4)$$

the equation for which can be written as:

$$\frac{\partial C_j}{\partial t} = -\frac{\rho}{\phi} \left[k_{j1} \left(K_{j1} C_j \left(s_{j1}^{\max} - \sum_{n=1}^{\infty} s_{n1} \cdot \frac{\sigma_n}{\sigma_j} \right) \right) + k_{j2} \left(K_{j2} C_j \left(s_{j2}^{\max} - \sum_{n=1}^{\infty} s_{n2} \cdot \frac{\sigma_n}{\sigma_j} \right) - s_{j2} \right) \right] \quad (5)$$

which follows from Eq. (3), with the added consideration for type of site indicated by either subscript 1 or 2. We add another stipulation that the adsorption reaction at Type 1 sites (zeolites) is irreversible; i.e., once adsorbed onto the zeolite, it is not released back into the mobile phase. That is, for Xe, as an example:



The monolayer is divided into Type 1 sites (Θ_1) and Type 2 sites (Θ_2) such that $\Theta_1 + \Theta_2 = \Theta_{\text{mono}} = 1$.

We chose to model adsorption to zeolitic sites as irreversible based on the assumption that the zeolite cages do not readily relinquish adsorbed molecules once taken into their structure. Similar behavior was noted by Seoung et al. (2014) under relatively high pressures (~0.1 GPa). The relatively low temperature of the experiment likewise does not promote desorption. That being said, the choice of reversible versus irreversible kinetics proved inconsequential to the modeling results, as the experiments proceed “forward” only (i.e., cores initially have zero tracer concentration within, and are then exposed to tracers passing through) and for only a relatively short time frame (20 h). Work by Feldman et al. (2020) determined that irreversible bonds between noble gases and zeolite adsorption sites is not expected – though they note that the desorption is not instantaneous – and that desorption is likely to occur if the rock is exposed to alternating high and low tracer concentrations, such as in barometric pumping. This is an important general consideration, although as previously noted, our experiments proceed forward only, so the (ir)reversible kinetics assumption did not affect our results.

Even the dual-site adsorption model described above is somewhat idealized compared to the actual arrangement of adsorption sites that may be available in zeolitic rock. For example, the zeolite present in the our tuff sample (mordenite) has two channels, side pockets, and external surfaces, some or all of which could be accessible to trace gases. In the interest of simplicity and interpretability, we have chosen to represent all possible zeolitic pore adsorption sites with a single site type, and all non-zeolite adsorption sites with yet another single site type.

2.2.2. Governing equations

The governing equations for transport of a tracer gas with matrix adsorption in the diffusion cell are given by:

$$\frac{\partial}{\partial t} \left[(1 - S_w) \phi C_v + (1 - \phi) s \right] = \nabla \cdot \left[(1 - S_w) \phi D \nabla C_v \right] + \dot{m} \quad (6)$$

where t is time [s], C_v is vapor-phase tracer concentration [mol kg_v^{-1}], s is the adsorbed (solid-phase) concentration [mol kg_r^{-1}], S_w is the water saturation [–; m^3/m^3], defined as total water volume divided by total pore volume, ϕ is the rock matrix porosity [–; m^3/m^3], and \dot{m} is the tracer sink term [$\text{mol m}^{-3} \text{s}^{-1}$] which is prescribed as a boundary condition at the sampling nodes connected to the mass spectrometer (see Section 2.2.3). Vapor-phase concentration can also partition into the aqueous phase according to Henry's law assuming equilibrium conditions: $C_v = \frac{C_{aq}}{k_H} \frac{1}{RT \rho_v}$, where k_H° is the so-called Henry solubility constant in water [$\text{mol}/(\text{kg} \cdot \text{bar})$], C_{aq} is the concentration of the species in the aqueous phase [mol kg_w^{-1}], R is the universal gas constant, T is temperature [K], and ρ_v is gas density [kg m^{-3}]. Henry's law solubility coefficients are given in the Supporting Information (Table S1). The transport of tracer that has partitioned into the aqueous phase is given by:

$$\frac{\partial}{\partial t} [S_w \phi C_{aq}] = \nabla \cdot (S_w \phi D_l \nabla C_{aq}) \quad (7)$$

where D_l is the liquid-phase diffusion coefficient [$\text{m}^2 \text{s}^{-1}$] of the species in an excess of water. We assume that no adsorption occurs in the aqueous phase, and note that the absence of the \dot{m} term since the sampling ports are located within the vapor-only chambers. Since concentrations are measured in the vapor phase, and because we assume that no adsorption occurs in the aqueous phase, C terms in the remainder of this paper section refer to vapor-phase concentration of the given tracer.

The total rate of formation of sorbed tracer of species j is given by:

$$\frac{\partial s_j}{\partial t} = \frac{\partial s_{j1}}{\partial t} + \frac{\partial s_{j2}}{\partial t} \quad (8)$$

where the rates of formation of the sorbed tracer for each site type follow from Eq. (5):

$$\frac{\partial s_{j1}}{\partial t} = k_{j1} K_{j1} C_j \left(s_{j1}^{\max} - \sum_{n=1}^{\infty} s_{n1} \cdot \frac{\sigma_n}{\sigma_j} \right) \quad (9)$$

and

$$\frac{\partial s_{j2}}{\partial t} = k_{j2} \left(K_{j2} C_j \left(s_{j2}^{\max} - \sum_{n=1}^{\infty} s_{n2} \cdot \frac{\sigma_n}{\sigma_j} \right) - s_{j2} \right) \quad (10)$$

where we again note that we have imposed the restriction that there is no desorption of species once adsorbed to Type 1 sites (i.e., zeolitic pores).

2.2.3. Initial and boundary conditions

The inlet chamber is spiked with an initial concentration of 2000 ppmv each of Xe, Kr, and SF₆. The initial gas tracer concentration is 0 ppmv elsewhere. Initial pressure in the diffusion cell is equal to the ambient atmospheric pressure everywhere ($P = 0.08 \text{ MPa}$). Exterior boundaries are all prescribed no-flux boundary conditions with regards to both fluid flow and tracer transport. The exception is at the sampling and inlet nodes, for which one of each is located in the inlet and outlet chambers (Fig. 2). The sampling node removes air and tracer mass from the chamber at a constant rate commensurate with the average sampling rate being pulled to the mass spectrometer (0.8 mL/h in the inlet chamber; 2.4 mL/h in the outlet chamber). The inlet node represents the needle valve in the experiment that prevents a vacuum from forming (Fig. 1), and replaces air in the chamber at a rate equivalent to the average sampling rate in the experimental procedure. As in the experimental setup, the sampling procedure removes tracer mass and air and replaces the mass with fresh air, the chambers become diluted with air as the experiment proceeds. Simulated concentrations are recorded at the sampling nodes.

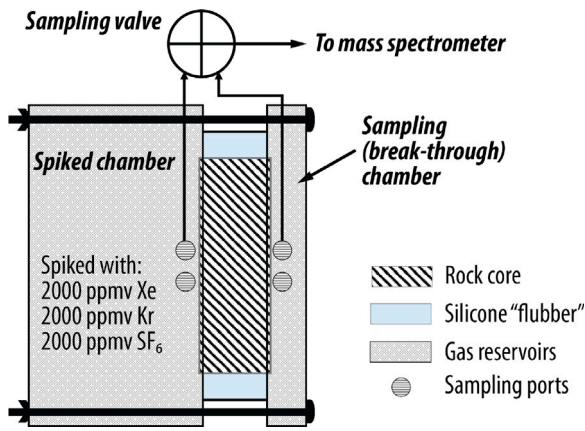


Fig. 1. Diffusion cell schematic.

2.2.4. Numerical model domain

The laboratory experiments were simulated using the Finite Element Heat and Mass (FEHM) transport simulator (Zyvoloski et al., 1999, 2021, 2017). A simple 1-dimensional mesh was generated assuming radial symmetry about the x -axis such that the 3-D volumes are preserved. A 1-D axially-symmetric geometry is ideal for representing the experimental setup because it preserves the cylindrical shape of the rock core sample and is dimensionally consistent in terms of volume and length. In the numerical domain, the spike (inlet) chamber, rock core, and sampling (outlet) chamber dimensions have the same radius, and the lengths of each chamber is adjusted such that the total volume is identical to the experimental setup. The mesh is uniformly discretized such that $\Delta x = \Delta r = 3.175$ mm (Fig. 2).

2.3. Parameter estimation

We use the differential evolution algorithm (Storn and Price, 1997) to find the transport parameters that produce a global minimum in root mean squared error (RMSE) when comparing the modeled break-through to the experimental results. Parameter estimation is performed in serial, starting with $S_w = 0\%$ and subsequently solving for parameters at progressively higher degrees of saturation. The optimization routine is constrained using both bounds and linear constraints following the approach by Lampinen (2002). The bounds for the parameters are as follow:

$$10^{-8} \leq D_j^* \leq 10^{-5} \text{ m}^2 \text{ s}^{-1}$$

$$10^{-6} \leq K_{j1} \leq 10^4 \text{ kg}_v \text{ mol}^{-1}$$

$$10^{-6} \leq K_{j2} \leq 10^4 \text{ kg}_v \text{ mol}^{-1}$$

$$10^{-3} \leq k_{j1} \leq 10^1 \text{ h}^{-1}$$

$$10^{-3} \leq k_{j2} \leq 10^1 \text{ h}^{-1}$$

$$10^0 \leq \text{SSA} \leq 10^{3.48} \text{ m}^2 \text{ kg}_r^{-1}$$

$$10^{-2} \leq \theta_1 \leq 10^{-0.52}$$

where the sampled porous media diffusion coefficient D_j^* ($= \frac{D_{j0}}{\tau}$; Eq. (1)) translates to the implicit range of effective diffusion coefficients, $D_{j,e}$:

$$10^{-9.52} \leq D_{j,e} \leq 10^{-5.69} \text{ m}^2 \text{ s}^{-1}.$$

As the parameter estimation proceeds to scenarios with increasing water saturation, we choose to force SSA to decrease as a direct result of increasing S_w , which is consistent with the expectation that in zeolites, increasing S_w decreases access to adsorption sites. The initial bounds for SSA of zeolitic tuff under dry ($S_w = 0\%$) conditions is $10^{2.95} \leq \text{SSA} \leq 10^{3.48} \text{ m}^2 \text{ kg}_r^{-1}$, consistent with the potential specific surface area values found for some tuffs (Reddy and Claassen, 1994). After $S_w = 0\%$, the bounds for SSA update such that the new upper bound is the solved parameter value from the previous S_w , and the lower bound is $1 \text{ m}^2 \text{ kg}_r^{-1}$. The upper bounds on θ_1 (0.30), the fraction of the total SSA comprised of Type 1 sites (zeolites), is chosen based on the approximate surface area of pores containing zeolites inferred in Supporting Information section 1. The parameters and bounds differed slightly for the non-zeolitic tuff and sandstone simulations, since a single-site competitive Langmuir adsorption reaction (Eq. (3)) was used rather than a dual-site model (Eq. (5)). The parameters solved for in these cases were: $D_{j,e}$, K_j , k , SSA. The bounds for these parameters were the same as their species-specific counterparts above, but we note that the same mass transfer rate constant (k) was used for each gas species.

To expedite the search through the solution space, we constrain the effective diffusion coefficient of each gas j to be within 1 order of magnitude (OOM) of each other species for a given S_w . This further facilitates the parameter estimation by being a reasonable approximation of the expected physics: the binary diffusion coefficients (D_{AB}) for the gases are relatively similar to each other (Table 1), as are the effective diffusion coefficients predicted by (Eq. (2)) at varying degrees of saturation (Table 1). The 1 OOM constraint on candidate values of D_e is conservative, and produces the expected result that the primary difference in transport between the gas species is determined by their relative affinity for the adsorbent rather than differences in diffusivity.

The global parameter space is quite large, and involves 7 free parameters each for 3 different gas species. Despite this, the differential evolution algorithm does a reasonable job of arriving at a single (though not unique) solution for the parameters that results in the lowest error. That being said, due to the high dimensionality of the problem, there may be many candidate solutions for the parameter

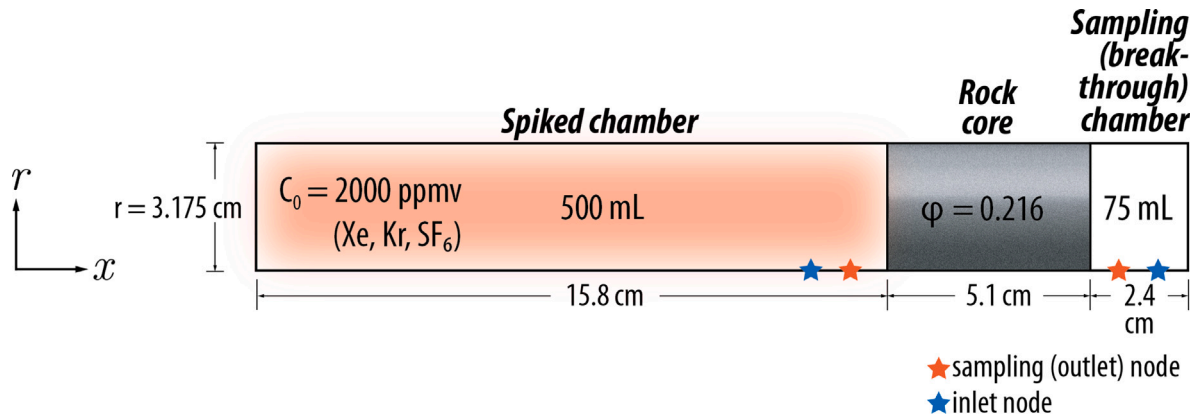


Fig. 2. Schematic of the 1-D axially-symmetric numerical model domain.

Table 1

Parameters used to calculate the binary diffusivity D_{AB}^{MQ} of each species with N_2 via Chapman-Enskog kinetic theory (Bird et al., 1960). Note that the σ terms in this table differ from σ_j in Eqs. (3), (5), (9), and (10) representing the area on an adsorbed molecule.

Gas	Chapman-Enskog parameters				D_{AB} [$m^2 s^{-1}$]
	M [g mol $^{-1}$]	σ [Å]	σ_{AB} [Å]	Ω_{AB} [-]	
Xe	131.293	4.009	3.838	1.087	1.58
Kr	83.798	3.675	3.675	1.030	1.91
SF ₆	146.06	5.205	4.436	1.096	1.16
N ₂	28.0134	3.667	–	–	–

choices that result in nearly identical errors. We want to examine such a candidate solution space to determine the degree to which we are confident in the estimated parameter values. To that end, we perform a second parameter search after the initial, large global search. The second search samples the subset of the initial global search containing solutions with the smallest errors (the “candidate solution space”). The second search is comparatively high-density in that the candidate solutions for each parameter cover a much smaller range than in the initial search. We again employ differential evolution within this space to refine the initial global solution, while also preserving the errors of all solutions *en route* for additional analysis. We call this second, refined search of the candidate solution space the high-density sampling.

3. Results

We present our simulations of the diffusion cell experiment and the derived diffusion and adsorption parameters estimated therein. Part of this work aims at determining how well the results compare to the commonly used MQ predictions of effective diffusivity (Eq. (2)) for variably saturated porous media. For comparison, we calculate the predicted MQ effective diffusivity using the binary diffusivity with N_2 from Chapman-Enskog kinetic theory (Bird et al., 1960):

$$D_{AB} = \frac{0.0018583}{P\sigma_{AB}^2\Omega_{AB}} \sqrt{T^3 \left(\frac{M_A + M_B}{M_A M_B} \right)} \quad (11)$$

where D_{AB} is the binary diffusion coefficient [$m^2 s^{-1}$] of two gases A and B in equal parts, P is the pressure [atm], σ is the collision diameter [Å], Ω_{AB} is the dimensionless collision integral, T is the temperature [K], and M_A and M_B are the molecular masses [g mol $^{-1}$] of species A and B , respectively. The binary diffusion coefficient D_{AB} is calculated for each of our gas species in equimolar quantities with N_2 . The Chapman-Enskog parameters used as well as the resulting binary diffusivity and tabulated free-air diffusivity are presented in Table 1.

The effective diffusivity (D_e) we calculate is derived from the flux calculations performed using Fick’s first law implemented within FEHM:

$$J = \theta_a D^* \nabla C \quad (12)$$

assuming the volumetric air content is not changing locally, where J is the solute flux [mol/(m 2 s)], C is concentration [mol kg $_v^{-1}$], θ_a is volumetric air content, and D^* is the porous medium diffusion coefficient, a quantity defined earlier in Eq. (1) that accounts for the tortuosity of the porous medium, which reduces the ability of a tracer to diffuse through the water in the pore spaces (Clennell, 1997). FEHM and other porous flow simulators generally use Eq. (12) for solute flux rather than one expressed in terms of effective diffusivity ($J = D_e \nabla C$), as it explicitly removes volumetric air content, isolating the diffusion coefficient that is experienced by chemicals within the air-filled pores (Ho and Webb, 1998). We therefore infer D_e from our simulations based on the sample porous medium diffusion coefficients (D^*), by the following relationship: $D_e = D^* \theta_a = D^* \phi(1 - S_w)$. We can therefore infer the tortuosity τ experienced by the gas tracers as they diffuse through the porous medium from the following relationship: $\tau = \frac{D_0}{D^*}$, as we have done in our Discussion of the results (Section 4).

3.1. Zeolitic tuff

The zeolitic tuff diffusion cell experiments were simulated numerically using the diffusive transport model with competitive dual-site kinetic Langmuir adsorption. Free parameters for each gas were: effective diffusion coefficient D_e , Langmuir distribution coefficients for Type 1 (K_{L1}) and Type 2 (K_{L2}) sites, reaction rate constants for Type 1 (k_1) and Type 2 (k_2) sites, specific surface area (SSA), and fractional coverage of Type 1 sites (θ_1). Sensitivity of the transport parameters to the degree of water saturation, S_w , was tested for at 0%, 17%, 40%, and 85% saturation.

Normalized breakthrough concentrations ($C(t)/C_0$, where $C(t)$ is the concentration in the breakthrough chamber and C_0 is the initial “spiked” concentration in the spiked chamber) of each gas are lower in the unsaturated ($S_w = 0\%$) case than at $S_w = 17\%$ (Fig. 3a,b). This is especially pronounced for xenon, which had breakthrough concentrations akin to those of the core when nearly fully saturated ($S_w = 85\%$; Fig. 3d). Such behavior departs considerably from that predicted based purely on porosity- and saturation-related tortuosity variations such as the MQ model (Eq. (2)). We note that because of the discrepancy of volumes between the inlet and outlet chambers, and that both chambers are normalized to the initial concentration in the inlet chamber only, the sum of normalized concentrations for both chambers is not equal to 1.0.

Despite the suppressed breakthrough concentrations, spiked chamber concentrations fall more rapidly and to a greater extent than at higher saturations, and to a much greater extent than they do for non-zeolitic tuff and sandstone. Relative concentration of Xe falls drastically during the unsaturated experiment, and especially quickly within the first 2-5 h. This implies that the gases (especially Xe) enter the core quickly, which is in contrast to the suppressed breakthrough concentrations in the sampling/breakthrough chamber.

Estimated parameter values are presented in Table 2, with estimated D_e summarized in Fig. 4. What is readily apparent from Fig. 4 is that the effective vapor-phase diffusion coefficients are much smaller than what is predicted based on tortuosity relationships, such as the MQ model. At $S_w = 0\%$, estimated D_e is less than D^{MQ} by at least 1 OOM. D_e also appears to increase slightly for Kr as saturation increases from 0 to 17%, which runs counter to the trend predicted by the MQ model. As progressively more water is added to the core, D_e begins to decrease. Nonetheless, the decrease in diffusivity is somewhat less noticeable than the nearly 2 OOM drop in diffusivity between $S_w = 0\%$ and 85% predicted by the MQ model.

The relative affinity of the individual gas species for adsorption to Type 1 sites (i.e., pores containing zeolites) is quantified by the distribution coefficient K_{L1} , in tandem with the reaction rate constant, k_1 (Eq. (5)). Under dry conditions ($S_w = 0\%$), the relative ranking of the magnitudes of K_{L1} went as: Xe \gg Kr \gg SF₆. Similarly, k_1 went as: Xe > Kr > SF₆. These results are compatible with the previous results of Feldman et al. (2020) reporting preferential adsorption of xenon relative to other noble gases under dry conditions at field scale.

When the saturation was increased to 17%, D_e increased slightly for Kr and fell slightly for Xe and SF₆. K_{L1} decreased significantly for all gas species, though K_{L1} for xenon remained much higher than the other constituents. This can also be observed in (Supporting Information Figure S5), which shows greatly reduced adsorption to Type 1 and Type 2 sites. As progressively more water was added to the core ($S_w = 40\%$ and 85%), D_e decreased for each gas.

3.2. Non-zeolitic tuff

The non-zeolitic tuff (Bandelier tuff, Qbt2) diffusion cell experiments were simulated using the diffusive transport model with competitive single-site kinetic Langmuir adsorption. Free parameters for each gas were effective diffusion coefficient D_e , Langmuir distribution coefficient K_L , reaction rate constant k , and specific surface area SSA.

Table 2

Estimated transport properties of individual gases in zeolitic tuff. Effective diffusion coefficients predicted using the MQ model (Eq. (2)) are included for reference, calculated using the binary gas diffusivity (D_{AB}^{MQ}). The right-most column contains normalized concentrations (C/C_0) calculated for the breakthrough (outlet) chamber at $t = 20$ hours for experimental data and simulation.

Gas	S_w [%]	D_{AB}^{MQ} [$m^2 s^{-1}$]	D_e [$m^2 s^{-1}$]	K_{L1} [$kg_g mol^{-1}$]	K_{L2} [$kg_g mol^{-1}$]	k_1 [1/h]	k_2 [1/h]	SSA [$m^2 kg_r^{-1}$]	C/C_0 (@ $t=20h$) (exp., model)
Xe	0	2.05×10^{-6}	$1.15 \cdot 10^{-7}$	$6.84 \cdot 10^{+3}$	$4.88 \cdot 10^{+3}$	$3.41 \cdot 10^{-1}$	$2.26 \cdot 10^{-3}$	3000	0.085, 0.070
Xe	17	1.10×10^{-6}	$9.70 \cdot 10^{-8}$	$2.09 \cdot 10^{+2}$	$3.17 \cdot 10^{+1}$	$5.62 \cdot 10^{-2}$	$2.31 \cdot 10^{-2}$	2116	0.362, 0.367
Xe	40	3.73×10^{-7}	$7.08 \cdot 10^{-8}$	$9.33 \cdot 10^{-2}$	$2.23 \cdot 10^{-2}$	$5.51 \cdot 10^{-2}$	$9.21 \cdot 10^{-2}$	1424	0.314, 0.328
Xe	85	3.67×10^{-9}	$1.76 \cdot 10^{-8}$	$4.31 \cdot 10^{-1}$	$9.87 \cdot 10^{+2}$	$4.98 \cdot 10^{-3}$	$7.90 \cdot 10^{-2}$	240	0.130, 0.136
Kr	0	2.47×10^{-6}	$1.09 \cdot 10^{-7}$	$2.14 \cdot 10^{+3}$	$2.49 \cdot 10^{-5}$	$2.51 \cdot 10^{-1}$	$9.79 \cdot 10^{+0}$	3000	0.323, 0.303
Kr	17	1.33×10^{-6}	$1.13 \cdot 10^{-7}$	$6.71 \cdot 10^{+1}$	$7.47 \cdot 10^{-2}$	$2.45 \cdot 10^{-2}$	$3.09 \cdot 10^{-1}$	2116	0.479, 0.497
Kr	40	4.51×10^{-7}	$7.18 \cdot 10^{-8}$	$6.61 \cdot 10^{-3}$	$7.25 \cdot 10^{-3}$	$2.01 \cdot 10^{+3}$	$1.88 \cdot 10^{-4}$	1424	0.414, 0.438
Kr	85	4.44×10^{-9}	$1.75 \cdot 10^{-8}$	$1.71 \cdot 10^{-1}$	$5.30 \cdot 10^{+2}$	$1.34 \cdot 10^{-3}$	$8.61 \cdot 10^{-2}$	240	0.202, 0.207
SF ₆	0	1.51×10^{-6}	$8.27 \cdot 10^{-8}$	$4.21 \cdot 10^{+0}$	$1.26 \cdot 10^{-3}$	$1.89 \cdot 10^{-1}$	$8.76 \cdot 10^{+0}$	3000	0.398, 0.398
SF ₆	17	8.09×10^{-7}	$7.74 \cdot 10^{-8}$	$8.05 \cdot 10^{-6}$	$3.05 \cdot 10^{-6}$	$4.98 \cdot 10^{-2}$	$7.09 \cdot 10^{+0}$	2116	0.501, 0.505
SF ₆	40	2.74×10^{-7}	$4.42 \cdot 10^{-8}$	$2.68 \cdot 10^{-1}$	$4.71 \cdot 10^{+0}$	$2.84 \cdot 10^{-3}$	$1.65 \cdot 10^{+0}$	1424	0.402, 0.421
SF ₆	85	2.70×10^{-9}	$9.87 \cdot 10^{-9}$	$5.06 \cdot 10^{+0}$	$4.68 \cdot 10^{+1}$	$5.15 \cdot 10^{-1}$	$4.89 \cdot 10^{+0}$	240	0.152, 0.152

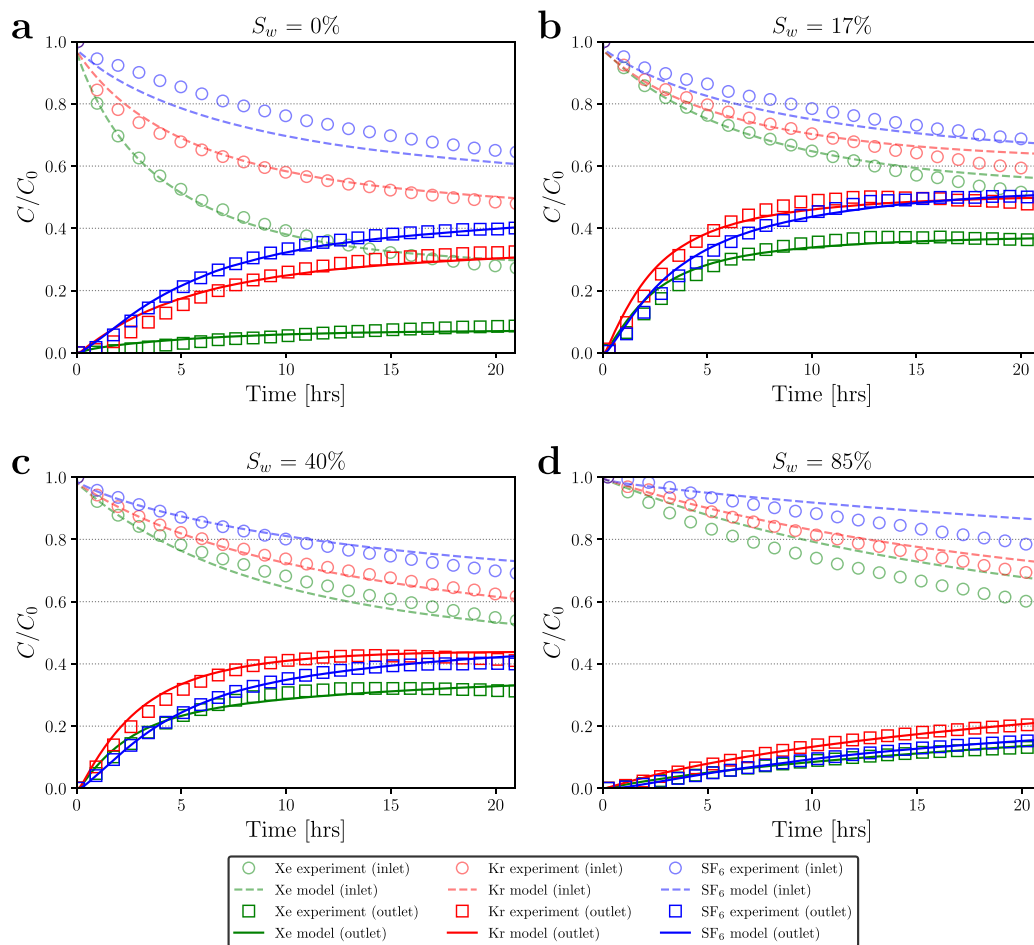


Fig. 3. Simulated concentration curves within the spiked and breakthrough chambers for each gas at each saturation in zeolitic tuff. Each panel letter corresponds to the titular degree of saturation (S_w).

Sensitivity of the transport parameters to the degree of water saturation, S_w , was tested for at 0% (Fig. 5a) and 27% (Fig. 6b) saturation. To simplify the analysis, we constrained the parameter search by fixing the reaction rate constant to be the same value for each gas at each saturation. We also constrained the Langmuir distribution coefficient (K_L) for each gas to be equal to the value estimated by the algorithm for the initial degree of saturation S_w . Therefore, after estimating parameters for $S_w = 0\%$, the only remaining free parameters were D_e and SSA. These constraints were found to not hinder convergence to a candidate solution space (Figures S20-S25).

In order of descending magnitude, the effective vapor-phase diffusion coefficients (D_e) rank as $Kr > Xe > SF_6$. This relationship was consistent for all S_w . The relative ranking of D_e between gases was consistent with the effective diffusivity predicted by the MQ model using estimated binary diffusion coefficients, D_{AB}^{MQ} (Eq. (11)).

As expected, D_e decreases as S_w increases. As S_w increases from 0% to 27%, the estimated D_e of each gas decreases by 60%–65%, depending on the particular species. The relative decrease in D_e determined in our simulations is approximately equivalent to the 65% decrease in D_{AB}^{MQ} predicted by the MQ model using binary diffusion coefficients.

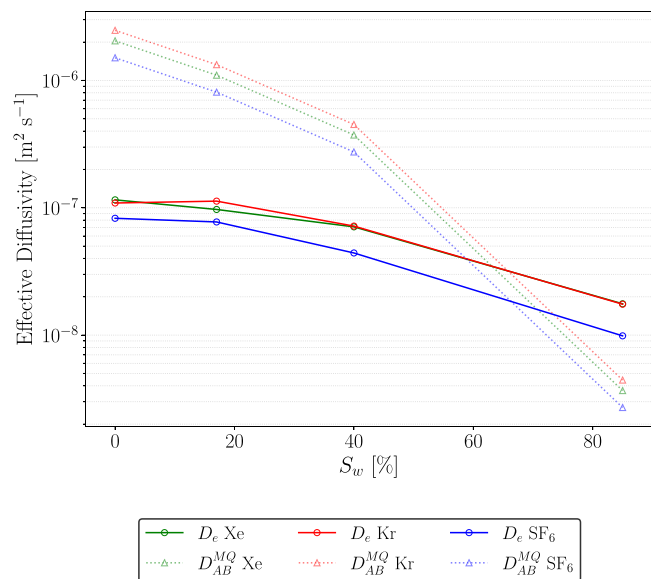


Fig. 4. Estimated D_e plotted against saturation, S_w for zeolitic tuff experiments (solid lines). Faded markers and dashed/dotted lines represent expected effective diffusivities based on the MQ model. The vertical axis has been plotted in logarithmic space to capture the large difference in magnitudes of expected D_{AB}^{MQ} and our calculated D_e .

A recent study (Neil et al., 2024) performed similar diffusion cell experiments testing temperature-dependence of diffusivity for Qbt2 cores. Calculating D_e from their reported D^* values yields D_e for Xe ($1.01 \times 10^{-6} \text{ m}^2 \text{ s}^{-1}$), Kr ($1.21 \times 10^{-6} \text{ m}^2 \text{ s}^{-1}$), and SF₆ ($7.74 \times 10^{-7} \text{ m}^2 \text{ s}^{-1}$) at 20 °C, which are relatively close to the values calculated in our study (Table 3) under dry conditions ($S_w = 0\%$); our estimated D_e values were between a factor of 1.2 and 1.4 greater than those calculated in Neil et al. (2024), which could be attributed to variations between core samples.

The specific surface area, SSA, decreases substantially between S_w 0% and 27%. The decrease in available sorptive SSA was 24.2%, which is roughly proportional to the increase in liquid saturation (27%) in the pore space. This relationship was also noticed in our analysis of surface area decrease with the addition of water observed in the SANS experiments (Figures S3, S4), though only in an approximate sense, and for a zeolitic sample. The percent decrease in pore surface area (SSA) filled (30%) in the non-zeolitic tuff is slightly less than the percent increase in S_w (27%). In terms of magnitude, while we do not have prior estimates of SSA for Bandelier tuff, previous research (Reddy and Claassen, 1994) of welded tuffs has found SSA values of about $2300 \pm 200 \text{ m}^2 \text{ kg}_r^{-1}$, so the dry condition values in Table 3 appear reasonable.

In order of decreasing magnitude, K_L ranked as Xe > Kr > SF₆. Although K_L and k were held constant between degrees of saturation, because the SSA decreases (and, therefore, the number of free sites) as water is added, the apparent adsorption likewise decreases as water prevents access to free sites – this can be seen in the mass loading (Figure S6).

The recent study (Neil et al., 2024) performed similar diffusion cell experiments on dry Qbt2 cores with the goal of determining temperature-dependent diffusion coefficients and adsorptivity for the same gas tracers investigated in our study. Their modeling investigation differed from ours in that they modeled tracer adsorption as a linear isotherm with a single parameter in the equilibrium distribution coefficient, K_d [kg_v/kg_r]. However, similar to the findings of our results, they determined that all three gas species undergo non-negligible adsorption at lower temperatures (20 °C), with decreasing magnitude of K_d going as Xe > Kr > SF₆. All three gas species had K_d of order 10^{-4} [kg_v/kg_r], where we note that values under 10^{-6} represent essentially non-sorbing conditions. Hence, our results corroborate other results for non-zeolitic

Table 3

Estimated transport properties of individual gases in non-zeolitic tuff. Effective diffusion coefficients predicted using the MQ model (Eq. (2)) are included for reference, calculated using the binary gas diffusivity (D_{AB}^{MQ}).

Gas	S_w [%]	D_{AB}^{MQ} [$\text{m}^2 \text{ s}^{-1}$]	D_e [$\text{m}^2 \text{ s}^{-1}$]	K_L [$\text{kg}_v \text{ mol}^{-1}$]	k [1/h]	SSA [$\text{m}^2 \text{ kg}_r^{-1}$]
Xe	0	$4.04 \cdot 10^{-6}$	$1.23 \cdot 10^{-6}$	$3.11 \cdot 10^3$	$2.88 \cdot 10^{-3}$	1527
Xe	27	$1.42 \cdot 10^{-6}$	$4.89 \cdot 10^{-7}$	$3.25 \cdot 10^3$	$2.88 \cdot 10^{-3}$	1066
Kr	0	$4.89 \cdot 10^{-6}$	$1.66 \cdot 10^{-6}$	$2.01 \cdot 10^3$	$2.88 \cdot 10^{-3}$	1527
Kr	27	$1.71 \cdot 10^{-6}$	$5.93 \cdot 10^{-7}$	$2.06 \cdot 10^3$	$2.88 \cdot 10^{-3}$	1066
SF ₆	0	$2.98 \cdot 10^{-6}$	$9.67 \cdot 10^{-7}$	$1.71 \cdot 10^3$	$2.88 \cdot 10^{-3}$	1527
SF ₆	27	$1.04 \cdot 10^{-6}$	$3.72 \cdot 10^{-7}$	$1.77 \cdot 10^3$	$2.88 \cdot 10^{-3}$	1066

Qbt2 tuff in that adsorption of these species is non-negligible (see Figure S6a,b).

3.3. Sandstone

The sandstone diffusion cell experiments were simulated using the diffusive transport model with competitive single-site kinetic Langmuir adsorption. Free parameters for each gas were effective diffusion coefficient D_e , Langmuir distribution coefficient K_L , reaction rate constant k , and specific surface area SSA. Transport parameters were estimated only at $S_w = 0\%$ (Fig. 6). Similar to the methods applied to the non-zeolitic tuff case, we simplified the analysis by constraining the parameter search by fixing the reaction rate constant at same value for each gas. Although we initially begin the parameter search with generically large range of values for SSA, in presenting the results below, we select the best solution from a subset of the candidate solution space (Figures S26-S27) where SSA is within the approximate range of realistic values for Castlegate sandstone ($\text{SSA} \leq 100 \text{ m}^2 \text{ kg}_r^{-1}$). Previous work (Fredrich et al., 2006) reported values of SSA for Castlegate sandstone between 13.4 and 21.1 mm^{-1} , for which assuming a density of $\sim 2694 \text{ kg m}^{-3}$ and the porosity of our sample yields a range of 49.7 to 78.3 $\text{m}^2 \text{ kg}_r^{-1}$.

In order of descending magnitude, the effective vapor-phase diffusion coefficients (D_e) ranked as Kr > Xe > SF₆ (see Table 4). The relative ranking between gases was consistent with the effective diffusivity predicted by the MQ model (Eq. (2)) using estimated binary diffusion coefficients (Eq. (11)), D_{AB}^{MQ} .

The recent study (Neil et al., 2024) performed similar diffusion cell experiments testing temperature-dependence of diffusivity for Berea sandstone, which had a porosity between 18%–20%. Our estimated D_e values were between a factor of 2.5 and 4.3 greater than those calculated in that study ($D_e(\text{Xe}) = 6.59 \times 10^{-7} \text{ m}^2 \text{ s}^{-1}$, $D_e(\text{Kr}) = 8.02 \times 10^{-7} \text{ m}^2 \text{ s}^{-1}$, $D_e(\text{SF}_6) = 5.26 \times 10^{-7} \text{ m}^2 \text{ s}^{-1}$). Higher estimates of D_e in our sandstone experiments (Table 4) are primarily due to the use of different rock units and the roughly 1.5 times greater porosity ($\phi = 28\%$) in the Castlegate sandstone in our investigation.

In order of decreasing magnitude, K_L ranked as Xe > Kr \approx SF₆. We were unable to represent the transport observed in the diffusion cell experiment for the Castlegate sandstone without enacting adsorption in our model (see Figure S7). This is consistent with results reported by Paul et al. (2018b), who found evidence for non-negligible adsorption of noble gases (including Xe) to Ottawa silica sand. Due to the relatively low SSA, the apparent adsorptivity in our experiments was fairly low overall (Figure S7).

4. Discussion

The experimental results reveal a clear and dramatic difference in variably-saturated diffusive-adsorptive transport behavior between rock types. Though one would not expect behavior to be universally applicable to different rock types, there is a great divergence from the behavior predicted by intuition and models such as MQ when zeolites are present in the rock pores. We discuss the experimental and

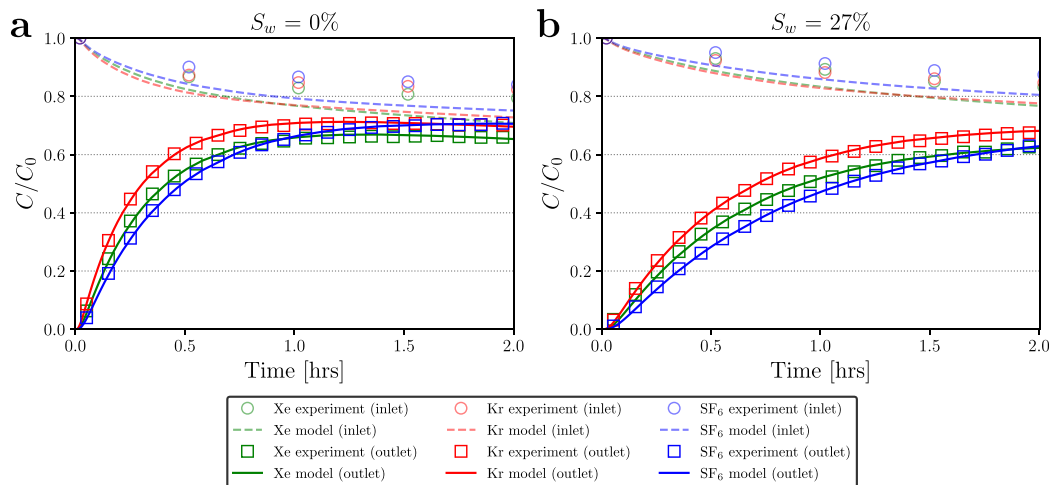


Fig. 5. Simulated concentration curves within the spiked and breakthrough chambers for each gas at each saturation in non-zeolitic tuff. Each panel letter corresponds to the titular degree of saturation (S_w).

Table 4

Estimated transport properties of individual gases in sandstone. Effective diffusion coefficients predicted using the MQ model (Eq. (2)) are included for reference, calculated using the binary gas diffusivity (D_{AB}^{MQ}).

Gas	S_w [%]	D_{AB}^{MQ} [$m^2 s^{-1}$]	D_e [$m^2 s^{-1}$]	K_L [$kg_m mol^{-1}$]	k [1/h]	SSA [$m^2 kg_r^{-1}$]
Xe	0	$2.89 \cdot 10^{-6}$	$1.72 \cdot 10^{-6}$	$8.84 \cdot 10^3$	$1.12 \cdot 10^{-2}$	100
Kr	0	$3.50 \cdot 10^{-6}$	$2.23 \cdot 10^{-6}$	$6.34 \cdot 10^3$	$1.12 \cdot 10^{-2}$	100
SF ₆	0	$2.13 \cdot 10^{-6}$	$1.34 \cdot 10^{-6}$	$6.26 \cdot 10^3$	$1.12 \cdot 10^{-2}$	100

Table 5

Effective diffusion coefficients and tortuosity values inferred from Eq. (1) for sandstone.

Gas	S_w [%]	D_e [$m^2 s^{-1}$]	τ_{AB} [-]
Xe	0	$1.72 \cdot 10^{-6}$	9.24
Kr	0	$2.23 \cdot 10^{-6}$	8.53
SF ₆	0	$1.34 \cdot 10^{-6}$	8.73

Table 6

Effective diffusion coefficients and tortuosity values inferred from Eq. (1) for non-zeolitic tuff.

Gas	S_w [%]	D_e [$m^2 s^{-1}$]	τ_{AB} [-]
Xe	0	$1.23 \cdot 10^{-6}$	12.87
Xe	27	$4.89 \cdot 10^{-7}$	32.28
Kr	0	$1.66 \cdot 10^{-6}$	11.53
Kr	27	$5.93 \cdot 10^{-7}$	32.20
SF ₆	0	$9.67 \cdot 10^{-7}$	12.01
SF ₆	27	$3.72 \cdot 10^{-7}$	31.23

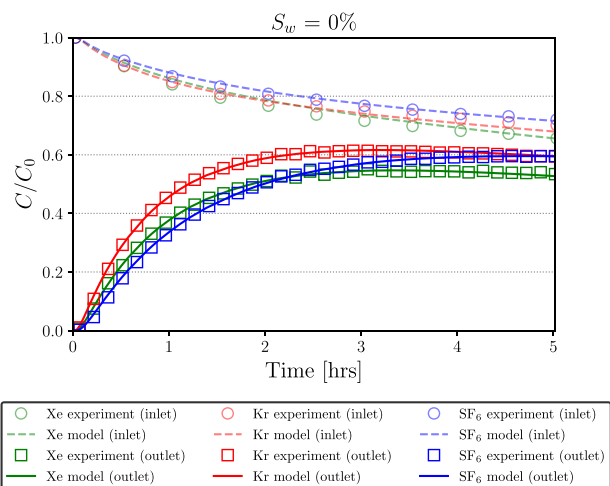


Fig. 6. Simulated concentration curves within the spiked and breakthrough chambers for each gas in sandstone.

modeling results starting with the most conventional (i.e., intuitive) results and progress to the most counter-intuitive behavior.

Diffusive transport through the Castlegate sandstone is very well approximated by the MQ model, such that the estimated D_e is within a few percent of D_{AB}^{MQ} for Xe and Kr. Because there was no pore water present, the pore tortuosity (τ) inferred from the estimated D_e (1) is relatively low ($5.6 < \tau < 11.3$; Table 5), depending on the free gas diffusivity used and can probably be entirely attributed to the porosity and pore connectivity. The gases generally did not adsorb much onto the pore walls, though it is worth noting that some adsorption was required in order to produce a good model fit.

Diffusive transport through the non-zeolitic tuff (Bandelier tuff, Qbt2) is also fairly well approximated by the MQ model. The magnitudes of D_e are smaller than those predicted by the MQ model using binary diffusivity (D_{AB}^{MQ}) by a factor of ~ 3 . The reduced diffusivity imparted by adding pore water is also well approximated by MQ; we observed a drop in D_e between 60%–65% depending on the gas species, which is very similar to the 65% percent reduction predicted by MQ. This decrease in D_e with increasing S_w is intuitive, as pore water reduces the effective volume in which gases can diffuse while also restricting travel to more tortuous pathways, as evidenced by the increasing values of τ in Table 6. As with the sandstone experiment, some adsorption was necessary in the model to produce a good fit to the data, though the number of moles adsorbed was relatively low compared to that in the zeolitic tuff.

The zeolitic tuff experiments show clearly the counter-intuitive behavior of the gas breakthrough concentration variations with increasing liquid saturation. Normalized breakthrough concentrations of each gas are lower in the unsaturated ($S_w = 0\%$) case than at $S_w = 17\%$ (Fig. 3a,b). This is especially exaggerated for Xe, which had breakthrough concentrations akin to those of the core when nearly fully saturated ($S_w = 85\%$; Fig. 3d). Such behavior departs considerably from that predicted based purely on porosity-saturation variations as in MQ. Apparently, conditions within the unsaturated core have a greater effect on diffusive transport of gaseous Xe than on the other gases studied.

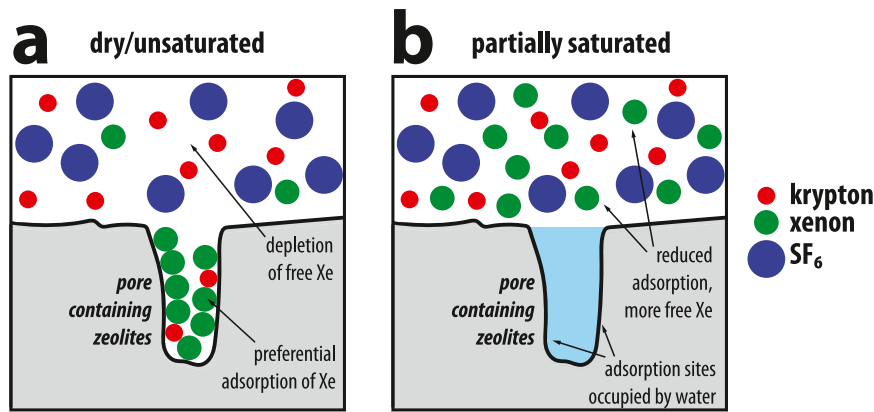


Fig. 7. Conceptual diagram showing how the addition of small amounts of water preferentially fills small pores containing zeolites, thereby reducing the adsorptive capacity of the rock. (a) Under dry (unsaturated) conditions, the zeolitic pores are accessible. Xe adsorbs strongly, and Kr adsorbs to a lesser degree, which reduces their gas-phase (“free”) concentrations in the pore spaces and retards transport; (b) when water is added, the zeolitic pores fill preferentially such that their adsorption sites become inaccessible to the gases. This increases the relative gas-phase concentration of Xe, reducing retardation.

This suppressed breakthrough behavior is even less intuitive when one considers the evolution of the spiked chamber concentrations in time. Normalized spiked chamber concentration of Xe falls drastically during the unsaturated experiment, and especially quickly within the first 2-5 h. This would seem to imply significant mass flux away from the spiked chamber into the rock core. However, as indicated by the greatly suppressed breakthrough concentrations, if the tracer mass is rapidly entering the core, the bulk of it is not passing through to the breakthrough chamber. To explain this behavior, we propose two phenomena that may be responsible: (i) very high adsorptive uptake via zeolitic pores having preference for the noble gases (xenon and, to a lesser extent, krypton), and (ii) high pore tortuosity resulting from pore-geometry effects, restricting diffusive transport despite relatively high total porosity.

4.1. Evidence for high adsorptive uptake by zeolitic pores

As previously stated in our conceptual model and discussion of the experimental results, which also appears in Neil et al. (2022a), there is experimental evidence implying that initial partial saturation up to at least $S_w = 17\%$ in zeolitic rock cores greatly reduces the interaction between zeolites and gas adsorbates. Our simulations indicate a substantial amount of adsorption of the noble gases (Xe, Kr) under dry conditions as the gas mixture diffuses through the core (Supporting Information Figure S5a). SF₆ mass loading is more than 2 OOM less than for the noble gases. When water is added, there was a substantial reduction in total mass adsorbed for each gas, pointing towards a correspondingly-reduced accessible volume for gas adsorption to occur. In contrast, in non-zeolitic tuff, we observed the expected behavior (progressively slower gas breakthrough as water is added) for gas diffusion, which lead us to hypothesize that the presence of zeolites greatly affects transport, and that the presence of water reduced the uptake of gases by the zeolites by blocking adsorption sites as the pores were filled. We attempt to illustrate this conceptual model in Fig. 7. This hypothesis was partially corroborated by small-angle neutron scattering (SANS) measurements performed on the zeolitic tuff samples (Fig. 5 in Neil et al., 2022a). The SANS measurements showed preferential filling of pore sizes suspected to be zeolites as small amounts of water were added to the sample (Figures S1, S2), which implies that adding water to the rock will block access to the zeolites and reduce gas adsorption, thereby resulting in reduced adsorptive retardation at higher liquid saturation.

The reduction of adsorptive capacity with saturation is reasonably well documented in previous studies of nanoporous materials (Lungu and Underhill, 1999; Hu et al., 2018a,b; Breck, 1974; Greathouse et al., 2023). Measurements of radioxenon adsorption on activated

carbon demonstrate that Xe adsorbed by saturated media decreases substantially, but does not diminish to zero (Lungu and Underhill, 1999). Nuclear Magnetic Resonance measurements performed using ¹²⁹Xe on nanoporous silicates during water adsorption and desorption have shown that some surface adsorption sites remain accessible even at high degrees of saturation, though in some cases the structure of the zeolite causes nearly all adsorbed xenon to be competitively displaced by water (Hu et al., 2018b). A study using molecular dynamics simulations and kinetic diffusion models determined that water molecules in zeolitic pores reduces gas loading and significantly slows the adsorption process (Greathouse et al., 2023). In general, the presence of water in zeolite pores will reduce the accessible volume for gas adsorption, which in turn reduces the mass that can be adsorbed by the zeolite.

High adsorptive uptake by zeolites could explain the rapid depletion of gas concentrations (and especially xenon) in the spiked chamber during the unsaturated core experiment. The rapid drop in concentrations within the spiked chamber is suggestive of high diffusive flux into the core. However, as is plainly evident in Fig. 3, concentrations in the breakthrough chamber are slow to build and highly suppressed relative to those at $S_w = 17\%$. Our model estimates D_e for each gas well below D^{M0} , which serves to explain the low breakthrough chamber concentrations, but not the rapid depletion in the spiked chamber. Strong adsorption, which is expected and apparently observed in this case, can cause similar behavior in fracture-matrix systems (Paul, 2017). In such systems, tracer gases are predicted to more rapidly diffuse into a highly adsorbent matrix, depleting the fracture of adsorbent tracers. The adsorption, which retards transport, does not increase diffusivity *per se*, however the diffusive flux is nevertheless enhanced by the preponderance of adsorption sites near the interface. This type of behavior is helpful in explaining the rapid depletion of concentrations in the spiked chamber despite relatively low D_e under dry conditions. It is compatible with the result that SF₆ had the fastest breakthrough, yet experienced the least amount of depletion in the spiked chamber. Krypton had the next fastest breakthrough, yet it experienced greater and more rapid depletion in the spiked chamber than SF₆ because it is expected to have greater adsorptive affinity for zeolites. With xenon having the highest adsorptive loading, its concentration in the spiked chamber decreases most rapidly, yet did not result in high breakthrough concentrations. When a small amount of water is added ($S_w = 17\%$), thereby reducing the adsorptive capacity of the rock, concentration depletion in the spiked chamber is reduced for all gases, though only marginally so for SF₆ due to having the lowest adsorptivity.

Adsorption is required to explain the observed behavior of the spiked chamber concentration depletion, and the greatly retarded transport of xenon despite its relatively high D_e . However, we require some other phenomenon to explain why still the estimated D_e of each gas

Table 7
Effective diffusion coefficients and tortuosity values inferred from Eq. (1) for zeolitic tuff.

Gas	S_w [%]	D_e [m ² s ⁻¹]	τ_{AB} [-]
Xe	0	$1.15 \cdot 10^{-7}$	29.55
Xe	17	$9.70 \cdot 10^{-8}$	29.18
Xe	40	$7.08 \cdot 10^{-8}$	28.89
Xe	85	$1.76 \cdot 10^{-8}$	29.03
Kr	0	$1.09 \cdot 10^{-7}$	37.84
Kr	17	$1.13 \cdot 10^{-7}$	30.36
Kr	40	$7.18 \cdot 10^{-8}$	34.46
Kr	85	$1.75 \cdot 10^{-8}$	35.38
SF ₆	0	$8.27 \cdot 10^{-8}$	30.35
SF ₆	17	$7.74 \cdot 10^{-8}$	26.92
SF ₆	40	$4.42 \cdot 10^{-8}$	34.09
SF ₆	85	$9.87 \cdot 10^{-9}$	38.15

is much lower than that predicted by MQ. Added to this question is why krypton – which as the smallest molecule should have the highest diffusion coefficient according to the kinetic theory of gases – was estimated to have the lowest D_e under dry conditions, and the highest D_e at all other degrees of saturation. For this, we look to pore geometry effects as potentially influencing the relative tortuosity experienced by each gas.

4.2. Influence of pore-geometry effects on effective diffusion coefficient

After isolating the effects of adsorption in our model, we were able to estimate D_e for each gas to reasonable degree of certainty. The candidate solution space for adsorptive parameters (e.g., $K_{L1,2}$, $k_{1,2}$) generally is not well constrained (Supporting Information section 3; Figures S8-S19) since there are many combinations that can produce similar responses in terms of adsorptive mass loading. It is encouraging that despite this, the range of values of D_e for each gas at each saturation is relatively well-constrained within this space. That is to say, for adsorption, we have a good idea of the overall adsorptive behavior of each gas, but not the values for each individual parameter. For D_e , on the other hand, we have a reasonably high confidence in the values obtained for each gas at each saturation.

What is apparent about the effective diffusivity within this zeolitic tuff is that it is much smaller than expected based on the MQ porosity-tortuosity relationship. At $S_w = 0\%$, where the difference is greatest, D_e is more than 1 OOM slower than D^{MQ} (Table 2). Another way of comparing the D_e estimated in our model with predicted D^{MQ} is to analyze the inferred tortuosity (τ) derived from Eq. (1). Recall from Eq. (1) that $\tau = D_0/D_e$. For sandstone, τ ranged from 5.6–11.3 (Table 5), and for non-zeolitic tuff, τ ranged from 7.8–15.5 at $S_w = 0\%$ and from 19.6–40.3 at $S_w = 27\%$ (Table 6). In zeolitic tuff, τ ranged from 18–39.2 at $S_w = 0\%$ to 17.6–49.3 at $S_w = 85\%$ (Table 7). Therefore, the inferred tortuosity within zeolitic tuff is higher than for non-zeolitic tuff and sandstone, and much greater than that implied by porosity-saturation relationships such as MQ.

Another point made apparent in the results from the zeolitic tuff experiments is that under dry conditions, the estimated D_e for the gases no longer preserve the relative ranking that follows from kinetic theory of gases. The relationship of kinetic diameters for each gas goes as: SF₆ (5.5 Å) > Xe (3.96 Å) > Kr (3.6 Å) (Breck, 1974; Marrero and Mason, 1972). So whereas D_e in both sandstone and non-zeolitic tuff follows this relationship, the estimated D_e for dry zeolitic tuff goes as Xe > SF₆ > Kr. It is notable that the gas with the smallest kinetic diameter (Kr) goes from having the highest diffusion coefficient (as follows from kinetic theory of gases) to having the second smallest effective diffusivity. Once water is added, however, Kr has highest D_e . An explanation may lie in the effect of pore size and geometry.

Variations in pore geometry and connectivity may contribute to increased tortuosity. The presence of very small pores or dead-end

pores can effectively increase the tortuosity of the pore space as long as gas molecules are able to access them. Previous research by Wu et al. (2019) found that porosity is not a reliable indicator of D_e , especially in porous structures with low D_e , because transport is hindered by dead-end or trapped pores and other complex features. They found that the net transport through samples with these types of complex features was dictated by a few of the narrowest pore throats along long, tortuous pathways. It is quite possible that the zeolitic tuff sample used in our experiments has just such a distribution of pore sizes and dead-end pores as to create highly tortuous conditions.

Zeolites have been documented as having a high proportion of nanopores and micropores (Greathouse et al., 2023; Feldman et al., 2020). Some of these contain the zeolite cages themselves, while others exist as crystallographic structures from related minerals within the rock. Mordeinite, the type of naturally-occurring zeolite present in our zeolitic tuff sample, has several pore types, but pores along the primary diffusion pathways have consistent diameter (6.5 Å; Simoncic and Armbruster (2004)) larger than the noble gases ($d_{Kr} = 3.6$ Å; $d_{Xe} = 3.96$ Å) and generally larger than SF₆ ($d_{SF6} = 5.5$ Å) (Breck, 1974). Other mordeinite pores have smaller pore diameters at the cage window, and still other non-zeolite pores exist in the natural rock sample. Dead-end pores contribute to the total porosity of the rock, but not to the connectivity between pores. The presence of dead-end pores increases the tortuosity within porous media because tracers can become temporarily entrapped within them before finding their way back out to the main connected pore volume. If such pores have pore throats with diameter smaller than the kinetic diameter of certain gas molecules, those molecules will be not be admitted, and the effective length of travel paths will consequently be shorter than molecules able to access the dead-end pores (Table 7). We illustrate this conceptual model in Fig. 8a, wherein the smallest gas species (Kr) is able to access the tight dead-end pores while larger species (Xe, SF₆) are blocked due to the pore-limiting windows. Consequently, the rate of passage of Kr is slowed due to the added tortuosity of its aggregate travel path, resulting in a lower inferred D_e . When water is added (Fig. 8b), it fills the small pores and prevents any gas from accessing the dead-end cul-de-sacs, reducing the effective tortuosity of the smaller gases. Under these conditions, the higher relative D_e for the smaller Kr is correctly predicted by kinetic theory of gases.

It is important to note that the presence of dead-end and nanopores is merely a part of the story in inferring the tortuosity of the porous medium. This is apparent in that for the zeolitic tuff, the highest calculated τ is experienced by SF₆, followed by Kr. Based on our conceptual model (Fig. 8), if the effect of nano-pores and dead-end pores was the only contributor to the total tortuosity, we would expect Kr to experience the greatest values of τ . However, what is noticeable is the relative difference in τ for Kr compared to Xe within the zeolitic tuff (Table 7) in contrast with the non-zeolitic tuff (Table 6) and sandstone (Table 5). The ratio of τ^{Kr}/τ^{Xe} in non-zeolitic tuff and sandstone is approximately 1.04 and 1.07, respectively. In zeolitic tuff this ratio is ~ 1.49 , which suggests that there are additional factors contributing to a nearly 50% greater tortuosity for Kr compared to the similarly-sized Xe beyond merely the differences in air-filled porosity.

There is some evidence in the literature supporting this type of pore-limiting behavior as causing higher D_e for smaller gas molecules. Molecular dynamics simulations in bulk mineral models have revealed that gas-adsorbent interactions and pore size can significantly reduce gas diffusion relative to that of the bulk gas (Dutta and Bhatia, 2019), and that these effects are pronounced within zeolites in particular (Dutta and Bhatia, 2018). A computational screening study of siliceous zeolites showed that zeolites containing narrow pores with tortuous diffusion pathways were effective at separating Xe/Kr from mixtures (Lawler et al., 2016). An in-depth study by Greathouse et al. (2023) used experiments and molecular dynamics simulations to quantify gas adsorptive loading and mobility in bulk zeolite slab models. That work found that smaller gases (Ar and Kr) were able

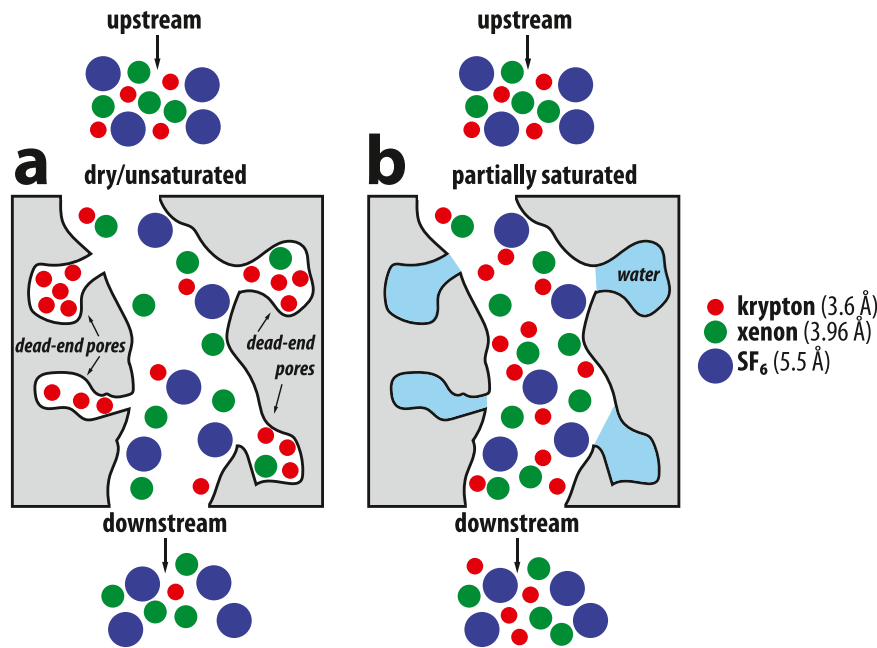


Fig. 8. Conceptual diagram of the effect of small dead-end pores increasing the effective tortuosity experienced by smaller gases (i.e., Kr) able to fit through the tight pore windows relative to larger gases (i.e., Xe and SF₆). (a) Under dry (unsaturated) conditions, the dead-end pores are accessible to Kr, causing it to have a low D_e relative to the larger gases despite having a smaller kinetic diameter; (b) when water is added, small pores fill with water and become inaccessible to the gases. Note that this diagram describes this tortuosity phenomenon which may effect the effective diffusion coefficient D_e of the gases, but does not describe the effects of adsorption of gases to zeolites or pore walls.

to access the zeolite interior, whereas larger gases (Xe and Rn) were effectively blocked from entering the bulk region of the zeolite by pore-limiting windows. In that study, the smaller gases were consequently reported as having increased mobility relative to the larger gases within pure zeolite slabs. An important distinction must be made, however, between definitions of “mobility” between the nano- and micro-scale characterization in Greathouse et al. (2023) and what we would consider as mobility at the meso-scale of our study. In molecular dynamics studies of zeolite slabs, mobility connotes greater access of gases to the interior of the bulk zeolite, which contains nano-scale pores and tortuous pathways – well within the regime of Knudsen diffusion. In our meso-scale model, we expect such mobility to decrease the overall rate at which mass can be delivered through the porous medium due to the aforementioned increase in access to highly tortuous pore volumes. Larger gas molecules (Xe and SF₆) with less ability to access interior nano-pores consequently have higher D_e under these conditions. When Greathouse et al. (2023) introduced water into their model, not only was there reduced gas loading onto zeolites via adsorption, but mobility by their definition was reduced as well, which fits the narrative illustrated in Fig. 8.

On the topic of Knudsen diffusion, we acknowledge the potential relevance of Knudsen diffusion and transition regime effects. While we do not have measurements of the full pore and pore-throat size distribution across nano- to meso-scale for this tuff, the implied preponderance of nanopores and the much lower than predicted D_e values could indicate that diffusion is taking place in the transition regime, which marks an intermediate regime between pure Knudsen diffusion and bulk diffusion. In such a regime, gas-solid interactions may dominate. Models such as dusty gas models calculate the effective diffusivity explicitly based on contributions from both the bulk diffusivity and the Knudsen diffusivity. Our choice of flow and transport simulator (FEHM) does not currently have the capability to explicitly separate bulk diffusion from Knudsen diffusion; as such, a detailed analysis using the dusty gas model or similar framework falls outside the scope of the present study. Nonetheless, the effective diffusion coefficient derived in our simulations can be interpreted as implicitly accounting for both bulk

and Knudsen diffusion effects. Future work could build on this study by incorporating more sophisticated models to explicitly resolve these contributions, which would provide a more detailed understanding of the transition flow regime.

5. Conclusions

This study investigates counter-intuitive transport behavior observed for gases in a variably-saturated rock core containing zeolites. A series of diffusion cell experiments measuring breakthrough for a gaseous mixture of Xe, Kr, and SF₆ were performed with progressively greater water saturation. Despite having high total porosity ($\phi \approx 22\%$), tracer breakthroughs and estimated effective vapor diffusion coefficients were found to be much smaller than what would be predicted by porosity- and saturation-based models such as the Millington-Quirk model. Breakthrough in dry conditions was exceptionally low for Xe even compared to the other gas species, despite the observation that Xe concentration in the inlet chamber dropped much faster than for the other gas species, which implies rapid entry into the core. We attribute this to preferential adsorption of Xe by zeolites, which has been documented in other studies. Furthermore, tracer breakthrough actually increased when the core saturation was increased from 0% to 17%, again deviating from typically predicted behavior. We propose two phenomena responsible for these counter-intuitive results: the addition of small amounts of water to the core (1) preferentially fills pores containing zeolites, reducing the adsorptive capacity of the rock, and also (2) preferentially fills dead-end nano-pores, which reduces the very high pore tortuosity. We found support for (1) in a marked decrease in adsorptive loading as S_w increased from 0% to 17% (Figure S5) – especially at zeolitic sites – though this phenomenon alone was insufficient to explain the increased breakthrough concentrations and small effective diffusion coefficients. We found support for (2) by observing that, under dry conditions, the species with the smallest kinetic diameter (Kr) had a smaller effective diffusion coefficient than the larger species, which contradicts behavior predicted by kinetic gas theory and our observations of transport in non-zeolitic tuff and

sandstone. We attribute this behavior to the presence of nano-scale dead-end pores, a significant proportion of which have throat diameters that create entry barriers to the larger gas molecules, effectively increasing the relative tortuosity for Kr. When S_w was increased to 17% the smallest pores filled preferentially, reducing tortuosity and causing Kr to have the highest effective diffusivity as expected.

We developed a competitive two-site kinetic Langmuir adsorption process within a diffusive transport model in order to constrain relevant transport parameters associated with the experimental diffusion cell results. Using a parameter estimation algorithm, we constrained the individual effective vapor-phase gas diffusion coefficients for each gas species to within a reasonable degree of certainty. We also characterized bulk changes in adsorptive behavior in zeolitic tuff with increasing water saturation, though the confidence in individual adsorption parameters (e.g., K_L , k) is comparatively lower. Our results reiterate previous findings (Greathouse et al., 2023; Lungu and Underhill, 1999) that adsorptive capacity of zeolites is greatly reduced upon partial saturation with water. These findings can be applied to historical UNE tracer test data and predictive transport models of mixed-gas transport in variably saturated zeolitic rock.

Future work will aim to further constrain the individual adsorption parameters contributing to the observed behavior using a physics-based approach. Due to the very large initial parameter space included in the search and comparatively lengthy computation time for the dual-site competitive adsorption simulations, candidate solutions for the adsorption parameters are still not well-constrained. Insights provided by the candidate solutions explaining adsorptive behavior provided by this research in conjunction with physical intuition will allow us to more rigorously constrain individual adsorption parameters and assist in the application of our model to predictive transport simulations.

CRedit authorship contribution statement

John P. Ortiz: Writing – original draft, Visualization, Software, Resources, Investigation, Formal analysis, Conceptualization. **Chelsea W. Neil:** Writing – review & editing, Resources, Methodology, Investigation, Data curation. **Harihar Rajaram:** Writing – review & editing, Supervision, Resources, Investigation, Formal analysis. **Hakim Boukhalfa:** Writing – review & editing, Resources, Methodology. **Philip H. Stauffer:** Writing – review & editing, Supervision, Resources, Methodology, Conceptualization.

Declaration of competing interest

The authors declare that they have no known competing financial interests or personal relationships that could have appeared to influence the work reported in this paper.

Acknowledgments

This Low Yield Nuclear Monitoring (LYNM) research was funded by the National Nuclear Security Administration, Defense Nuclear Non-proliferation Research and Development, USA (NNSA DNN R&D) by grant number LA21-V-LYNM-Containment-NDD2Fe. This manuscript has been authored with number LA-UR-24-28494 by Triad National Security under Contract with the U.S. Department of Energy, contract no. 89233218CNA000001. We gratefully acknowledge two anonymous reviewers, who contributed a thoughtful and thorough analysis of the manuscript with suggestions for revision and clarification.

The authors dedicate this work to the memory of our friend, colleague, and advisor, Harihar Rajaram (1965–2024).

Appendix A. Supplementary data

Supplementary material related to this article can be found online at <https://doi.org/10.1016/j.jenvrad.2024.107608>.

Data availability

Data will be made available on request.

References

- Ackley, M.W., Rege, S.U., Saxena, H., 2003. Application of natural zeolites in the purification and separation of gases. *Microporous Mesop. Mater.* 61, 25–42. [http://dx.doi.org/10.1016/S1387-1811\(03\)00353-6](http://dx.doi.org/10.1016/S1387-1811(03)00353-6).
- Adamson, A.A., 1979. *A Textbook of Physical Chemistry*, second ed. Academic Press, <http://dx.doi.org/10.1016/B978-0-12-044262-1.50028-1>.
- Auer, L.H., Rosenberg, N.D., Birdsell, K.H., Whitney, E.M., 1996. The effects of barometric pumping on contaminant transport. *J. Contam. Hydrol.* 24, 145–166.
- Avendaño, S.T., Harp, D.R., Kurwadkar, S., Ortiz, J.P., Stauffer, P.H., 2021. Continental-scale geographic trends in barometric-pumping efficiency potential: A North American case study. *Geophys. Res. Lett.* 48, 1–10. <http://dx.doi.org/10.1029/2021gl093875>.
- Baehr, A.L., 1987. Selective transport of hydrocarbons in the unsaturated zone due to aqueous and vapor phase partitioning. *Water Resour. Res.* 23, 1926–1938. <http://dx.doi.org/10.1029/WR023i010p01926>.
- Bird, R.B., Stewart, W.E., Lightfoot, E.N., 1960. *Transport Phenomena*. John Wiley & Sons.
- Bourret, S.M., Kwicklis, E.M., Harp, D.R., Ortiz, J.P., Stauffer, P.H., 2020. Beyond Barnwell: Applying lessons learned from the Barnwell site to other historic underground nuclear tests at Pahute Mesa to understand radioactive gas-seepage observations. *J. Environ. Radioact.* 222, 1–14. <http://dx.doi.org/10.1016/j.jenvrad.2020.106297>.
- Bourret, S.M., Kwicklis, E.M., Miller, T.A., Stauffer, P.H., 2019. Evaluating the importance of barometric pumping for subsurface gas transport near an underground nuclear test site. *Vadose Zone J.* 18, 1–17. <http://dx.doi.org/10.2136/vzj2018.07.0134>.
- Breck, D.W., 1974. *Zeolite molecular sieves: Structure, chemistry, and use*.
- Bruckler, L., Ball, B.C., Renault, P., 1989. Laboratory estimation of gas diffusion coefficient and effective porosity in soils. *Soil Sci.* 147, 1–10.
- Byers, M.F., Haas, D.A., Barth, B.S., Lowrey, J., 2019. Adsorption of tracer gases in geological media: Experimental benchmarking. *J. Radioanal. Nucl. Chem.* 322, 1621–1626. <http://dx.doi.org/10.1007/s10967-019-06768-3>.
- Carrigan, C.R., Heinle, R.A., Hudson, G.B., Nitao, J.J., Zucca, J.J., 1996. Trace gas emissions on geological faults as indicators of underground nuclear testing. *Nature* 382, 528–531. <http://dx.doi.org/10.1038/382528a0>.
- Carrigan, C.R., Sun, Y., 2014. Detection of noble gas radionuclides from an underground nuclear explosion during a CTBT on-site inspection. *Pure Appl. Geophys.* 171, 717–734. <http://dx.doi.org/10.1007/s00024-012-0563-8>.
- Clenell, M.B., 1997. *Tortuosity: A Guide Through the Maze*, vol. 122, Geological Society, London, Special Publications, pp. 299–344. <http://dx.doi.org/10.1144/GSL.SP.1997.122.01.18>.
- Conca, J.L., Wright, J., 2000. *Aqueous diffusion in the vadose zone*. In: Looney, B.B., Falta, R.W. (Eds.), *The Vadose Zone*. Battelle Press, Columbus, OH, pp. 796–797.
- Dutta, R.C., Bhatia, S.K., 2018. Interfacial barriers to gas transport in zeolites: Distinguishing internal and external resistances. *Phys. Chem. Chem. Phys.* 20, 26386–26395. <http://dx.doi.org/10.1039/c8cp05834b>.
- Dutta, R.C., Bhatia, S.K., 2019. Interfacial barriers to gas transport: Probing solid-gas interfaces at the atomistic level. *Mol. Simul.* 45, 1148–1162. <http://dx.doi.org/10.1080/08927022.2019.1635694>.
- Feldman, J., Paul, M., Xu, G., Rademacher, D.X., Wilson, J., Nenoff, T.M., 2020. Effects of natural zeolites on field-scale geologic noble gas transport. *J. Environ. Radioact.* 220–221, 106279. <http://dx.doi.org/10.1016/j.jenvrad.2020.106279>.
- Fredrich, J.T., DiGiovanni, A.A., Noble, D.R., 2006. Predicting macroscopic transport properties using microscopic image data. *J. Geophys. Res. Solid Earth* 111, <http://dx.doi.org/10.1029/2005JB003774>.
- Greathouse, J.A., Paul, M.J., Xu, G., Powell, M.D., 2023. Molecular dynamics simulation of pore-size effects on gas adsorption kinetics in zeolites. *Clays Clay Miner.* 71, 54–73. <http://dx.doi.org/10.1007/s42860-023-00231-x>.
- Harp, D.R., Ortiz, J.P., Pandey, S., Karra, S., Anderson, D.N., Bradley, C.R., Viswanathan, H.S., Stauffer, P.H., 2018. Immobile pore-water storage enhancement and retardation of gas transport in fractured rock. *Transp. Porous Media* 26, <http://dx.doi.org/10.1007/s11242-018-1072-8>.
- Ho, C.K., Webb, S.W., 1998. Review of porous media enhanced vapor-phase diffusion mechanisms, models, and data & #151; Does enhanced vapor-phase diffusion exist? *J. Porous Media* 1, <http://dx.doi.org/10.1615/JPorMedia.v1.i1.60>.
- Holmes, J.A., Lewis, S.R., Patel, M.R., 2015. Analysing the consistency of martian methane observations by investigation of global methane transport. *Icarus* 257, 23–32. <http://dx.doi.org/10.1016/j.icarus.2015.04.027>.
- Hu, W., Jiang, Y., Chen, D., Lin, Y., Han, Q., Cui, Y. and, 2018a. Impact of pore geometry and water saturation on gas effective diffusion coefficient in soil. *Appl. Sci. (Switzerland)* 8, <http://dx.doi.org/10.3390/app8112097>.
- Hu, Y., Li, M., Hou, G., Xu, S., Gong, K., Liu, X., Han, X., Pan, X., Bao, X., 2018b. The role of water in methane adsorption and diffusion within nanoporous silica investigated by hyperpolarized ^{129}Xe and ^1H PFG NMR spectroscopy. *Nano Res.* 11, 360–369. <http://dx.doi.org/10.1007/s12274-017-1638-8>.

- Jin, Y., Jury, W.A., 1996. Characterizing the dependence of gas diffusion coefficient on soil properties. *Soil Sci. Am. J.* 60, 66–71. <http://dx.doi.org/10.2136/sssaj1996.0361599500600010012x>.
- Johnson, C., Aalseth, C.E., Alexander, T.R., Bowyer, T.W., Chipman, V., Day, A.R., Drellack, S., Fast, J.E., Fritz, B.G., Hayes, J.C., Huckins-Gang, P., Kirkham, R.R., Lowrey, J.D., Mace, E.K., Mayer, M.F., McIntyre, J.I., Milbrath, B.D., Panisko, M.E., Paul, M.J., Obi, C.M., Okagawa, R.K., Olsen, K.B., Ripplinger, M.D., Seifert, A., Suarez, R., Thomle, J., Townsend, M.J., Woods, V.T., Zhong, L., 2019. Migration of noble gas tracers at the site of an underground nuclear explosion at the Nevada National Security Site. *J. Environ. Radioact.* 208–209, 106047. <http://dx.doi.org/10.1016/j.jenvrad.2019.106047>.
- Jordan, A.B., Stauffer, P.H., Zvyolloski, G.A., Person, M.A., MacCarthy, J.K., Anderson, D.N., 2014. Uncertainty in prediction of radionuclide gas migration from underground nuclear explosions. *Vadose Zone J.* 13, 1–13. <http://dx.doi.org/10.2136/vzj2014.06.0070>.
- Jury, W.A., Gardner, W.R., Gardner, W.H., 1991. *Soil Physics*. John Wiley & Sons, New York.
- Kalinowski, M.B., 2011. Characterisation of prompt and delayed atmospheric radioactivity releases from underground nuclear tests at Nevada as a function of release time. *J. Environ. Radioact.* 102, 824–836. <http://dx.doi.org/10.1016/j.jenvrad.2011.05.006>.
- Lampinen, J., 2002. A constraint handling approach for the differential evolution algorithm. In: *Proceedings of the 2002 Congress on Evolutionary Computation*, Vol. 2. CEC 2002, pp. 1468–1473. <http://dx.doi.org/10.1109/CEC.2002.1004459>.
- Lawler, K.V., Sharma, A., Alagappan, B., Forster, P.M., 2016. Assessing zeolite frameworks for noble gas separations through a joint experimental and computational approach. *Microporous Mesop. Mater.* 222, 104–112. <http://dx.doi.org/10.1016/j.micromeso.2015.10.005>.
- Lungu, C., Underhill, D., 1999. The effect of moisture on the adsorption of xenon by activated carbon. *Health Phys.* 77, 298–302. <http://dx.doi.org/10.1097/00004032-199909000-00008>.
- Marrero, T.R., Mason, E.A., 1972. Gaseous diffusion coefficients. *J. Phys. Chem. Ref. Data* 1, 3–118. <http://dx.doi.org/10.1063/1.3253094>.
- Massmann, J., Farrier, D.F., 1992. Effects of atmospheric pressures on gas transport in the vadose zone. *Water Resour. Res.* 28, 777–791. <http://dx.doi.org/10.1029/91WR02766>.
- Millington, R.J., Quirk, J.P., 1961. Permeability of porous solids. *Trans. Faraday Soc.* 57, 1200–1207.
- Moncure, G.K., Surdam, R.C., McKague, H.L., 1981. Zeolite diagenesis below pahute mesa, Nevada test site. *Clays Clay Miner.* 29, 385–396. <http://dx.doi.org/10.1346/CCMN.1981.0290508>.
- Mousis, O., Simon, J.M., Bellat, J.P., Schmidt, F., Bouley, S., Chassefière, E., Sautter, V., Quesnel, Y., Picaud, S., Lectez, S., 2016. Martian zeolites as a source of atmospheric methane. *Icarus* 278, 1–6. <http://dx.doi.org/10.1016/j.icarus.2016.05.035>, arXiv:1605.07579.
- Neeper, D.A., Stauffer, P.H., 2012a. Transport by oscillatory flow in soils with rate-limited mass transfer: 1. Theory. *Vadose Zone J.* 11, 1–14. <http://dx.doi.org/10.2136/vzj2011.0093>.
- Neeper, D.A., Stauffer, P.H., 2012b. Transport by oscillatory flow in soils with rate-limited mass transfer: 2. Field experiment. *Vadose Zone J.* 11, 1–12. <http://dx.doi.org/10.2136/vzj2011.0093>.
- Neil, C.W., Boukhalfa, H., Xu, H., Ware, S.D., Ortiz, J., Harp, D., Broome, S., Hjelm, R.P., Mao, Y., Avendaño, R., Brug, W.P., Stauffer, P.H., 2022a. Gas diffusion through variably-water-saturated zeolitic tuff: Implications for transport following a subsurface nuclear event. *J. Environ. Radioact.* 250, 106905. <http://dx.doi.org/10.1016/j.jenvrad.2022.106905>.
- Neil, C.W., Boukhalfa, H., Xu, H., Ware, S.D., Ortiz, J., Harp, D., Broome, S., Hjelm, R.P., Mao, Y., Avendaño, R., Brug, W.P., Stauffer, P.H., 2022b. Supporting information for: Gas diffusion through variably-water-saturated zeolitic tuff: Implications for transport following a subsurface nuclear event. *J. Environ. Radioact.* 250.
- Neil, C.W., Swager, K.C., Bourret, S.M., Ortiz, J.P., Stauffer, P.H., 2024. Rethinking porosity-based diffusivity estimates for sorptive gas transport at variable temperatures. *Environ. Sci. Technol.* <http://dx.doi.org/10.1021/acs.est.4c04048>.
- Nilson, R.H., Peterson, E.W., Lie, K.H., Burkhard, N.R., Hearst, J.R., 1991. Atmospheric pumping: A mechanism causing vertical transport of contaminated gases through fractured permeable media. *J. Geophys. Res. Solid Earth* 96, 933–948. <http://dx.doi.org/10.2752/147597509112541>.
- Ortiz, J.P., 2024. *Subsurface Flow and Transport Processes with Applications to Methane Variations on Mars* (Ph.D. thesis). The Johns Hopkins University, Baltimore, MD.
- Ortiz, J.P., Rajaram, H., Stauffer, P.H., Harp, D.R., Wiens, R.C., Lewis, K.W., 2022. Barometric pumping through fractured rock: A mechanism for venting deep methane to Mars' atmosphere. *Geophys. Res. Lett.* 49, e2022GL098946. <http://dx.doi.org/10.1029/2022GL098946>.
- Ortiz, J.P., Rajaram, H., Stauffer, P.H., Lewis, K.W., Wiens, R.C., Harp, D.R., 2024. Sub-diurnal methane variations on Mars driven by barometric pumping and planetary boundary layer evolution. *J. Geophys. Res. Planets* 129, e2023JE008043. <http://dx.doi.org/10.1029/2023JE008043>.
- Paul, M.J., 2017. *Transport and Sorption of Noble Gases in Porous Geological Media* (Ph.D. thesis). The University of Texas at Austin.
- Paul, M.J., Biegalski, S.R., Haas, D.A., Jiang, H., Daigle, H., Lowrey, J.D., 2018a. Xenon adsorption on geological media and implications for radionuclide signatures. *J. Environ. Radioact.* 187, 65–72. <http://dx.doi.org/10.1016/j.jenvrad.2018.01.029>.
- Paul, M.J., Biegalski, S.R., Haas, D.A., Lowrey, J.D., 2018b. Adsorptive transport of noble gas tracers in porous media. *Int. J. Modern Phys. Conf. Ser.* 48, 1860124. <http://dx.doi.org/10.1142/s2010194518601242>.
- Paul, M.J., Broome, S., Kuhlman, K.L., Feldman, J., Heath, J., 2020. An experimental method to measure gaseous diffusivity in tight and partially saturated porous media via continuously monitored mass spectrometry. *Transp. Porous Media* 133, 1–22. <http://dx.doi.org/10.1007/s11242-020-01397-x>.
- Pick, M.A., 1981. Kinetics of hydrogen absorption-desorption by niobium. *Phys. Rev. B* 24 (4287).
- Reddy, M.M., Claassen, H.C., 1994. Specific surface area of a crushed welded tuff before and after aqueous dissolution. *Appl. Geochem.* 9, 223–233. [http://dx.doi.org/10.1016/0883-2927\(94\)90008-6](http://dx.doi.org/10.1016/0883-2927(94)90008-6).
- Sallam, A., Jury, W.A., Letey, J., 1984. Measurement of gas diffusion coefficient under relatively low air-filled porosity. *Soil Sci. Am. J.* 48, 3–6. <http://dx.doi.org/10.2136/sssaj1984.03615995004800010001x>.
- Seoung, D., Lee, Y., Cynn, H., Park, C., Choi, K.Y., Blom, D.A., Evans, W.J., Kao, C.C., Vogt, T., Lee, Y., 2014. Irreversible xenon insertion into a small-pore zeolite at moderate pressures and temperatures. *Nature Chem.* 6, 835–839. <http://dx.doi.org/10.1038/nchem.1997>.
- Simoncic, P., Armbruster, T., 2004. Peculiarity and defect structure of the natural and synthetic zeolite mordenite: A single-crystal X-ray study. *Am. Mineral.* 89, 421–431.
- Stauffer, P.H., Rahn, T.A., Ortiz, J.P., Salazar, L.J., Boukhalfa, H., Behar, H.R., Snyder, E.E., 2019. Evidence for high rates of gas transport in the deep subsurface. *Geophys. Res. Lett.* 46, 3773–3780. <http://dx.doi.org/10.1029/2019GL082394>.
- Stauffer, P.H., Vrugt, J.A., Turin, H.J., Gable, C.W., Soll, W.E., 2009. Untangling diffusion from advection in unsaturated porous media: Experimental data, modeling, and parameter uncertainty. *Vadose Zone J.* 8, 510–522. <http://dx.doi.org/10.2136/vzj2008.0055>.
- Storn, R., Price, K., 1997. Differential evolution – A simple and efficient heuristic for global optimization over continuous spaces. *J. Global Optim.* 11, 341–359. <http://dx.doi.org/10.1023/A:1008202821328>.
- Sun, Y., Carrigan, C.R., 2014. Modeling noble gas transport and detection for the comprehensive nuclear-test-ban treaty. *Pure Appl. Geophys.* 171, 735–750. <http://dx.doi.org/10.1007/s00024-012-0514-4>.
- Takle, E.S., Massman, W.J., Brandle, J.R., Schmidt, R.A., Zhou, X., Litvina, I.V., Garcia, R., Doyle, G., Rice, C.W., 2004. Influence of high-frequency ambient pressure pumping on carbon dioxide efflux from soil. *Agricult. Forest. Meteorol.* 124, 193–206. <http://dx.doi.org/10.1016/j.agrformet.2004.01.014>.
- Wu, H., Fang, W.Z., Kang, Q., Tao, W.Q., Qiao, R., 2019. Predicting effective diffusivity of porous media from images by deep learning. *Sci. Rep.* 9, 20387. <http://dx.doi.org/10.1038/s41598-019-56309-x>.
- Zvyolloski, G.A., Robinson, B.A., Dash, Z.V., Chu, S., Miller, T.A., 2017. FEHM: Finite element heat and mass transfer code. [Software] GitHub.
- Zvyolloski, G.A., Robinson, B.A., Dash, Z.V., Kelkar, S., Viswanathan, H.S., Pawar, R.J., Stauffer, P.H., Miller, T.A., Chu, S., 2021. Software users manual (UM) for the FEHM application version 3.1-3X.
- Zvyolloski, G.A., Robinson, B.A., Dash, Z.V., Trease, L.L., 1999. *Models and Methods Summary for the FEHM Application*. Technical Report, Los Alamos National Laboratory, Los Alamos, NM.